Cryo-SPD, Microstructures, Properties of Metallic Nanomaterials at Low Temperatures

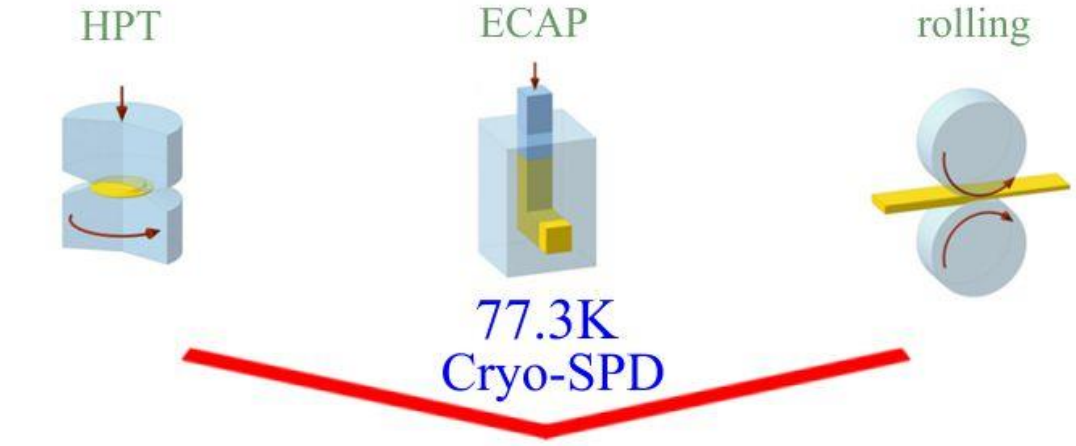

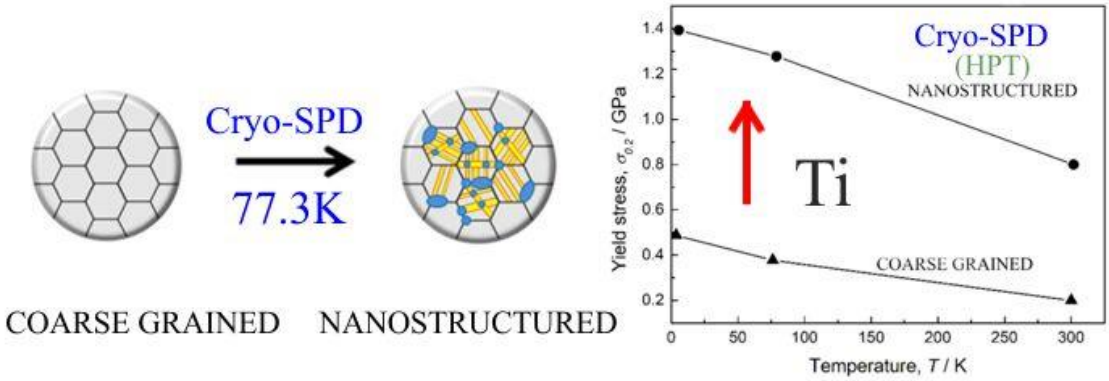

Cryo-Severe Plastic Deformation, Microstructures and Properties of Metallic Nanomaterials at Low Temperatures

Elena Tabachnikova[1], Tetiana Hryhorova[1], Sergii Shumilin[1], Yuriy Semerenko[1], Yi Huang[2,3], Terence G. Langdon[3]

[1]*B.Verkin Institute for Low Temperature Physics and Engineering of NAS of Ukraine,47 Nauky Ave., Kharkiv, 61103, Ukraine*

[2]*Department of Design and Engineering, Faculty of Science and Technology, Bournemouth University, Poole, Dorset BH12 5BB, UK*

[3]*Materials Research Group, Department of Mechanical Engineering, University of Southampton, Southampton SO17 1BJ, UK*

Based on the experimental results obtained mainly by the authors, the effect of decreasing the temperature to 77 K using various methods of cryogenic severe plastic deformation (cryo-SPD), such as equal-channel angular pressing, high-pressure torsion, as well as large deformations in the form of cryorolling, on the mechanical properties and mechanisms of plastic deformation is investigated. The results are presented for deformation of a number of metals (titanium, zirconium, cobalt), Ni-18.75%Fe alloy and high-entropy alloys (HEA) $Al_{0.5}CoCrCuFeNi$, $CrMnFeCoNi_2Cu$, CoCrFeNiMn over a wide range of low temperatures. The efficiency of using cryo-SPD methods to increase their strength is demonstrated. The reasons for the paradoxical effect of cryo-SPD on the mechanical characteristics of some HEAs, which contradict the thermally-activated nature of plastic deformation, are analyzed. It is shown that the use of the thermal activation analysis method makes it possible to establish the most probable physical mechanisms that determine the plasticity of a wide class of materials in the coarse-grained and nanostructured states. The features of plastic

deformation of various metals and alloys in the coarse-grained and nanostructured states in the ultralow temperature range (4.2-0.5 K) are described.

Keywords: *cryo-severe plastic deformation, cryo-rolling, ultralow temperature, metallic alloys, high-entropy alloys, strength, ductility, thermally-activated deformation.*

1. Introduction

The development of new methods for obtaining high strength materials by grain refinement is one of the major goals of modern materials science. One way to solve this problem is to use severe plastic deformation (SPD). Large plastic deformations ("top-down" deformations) during SPD, grains are refined to the submicron or nanometer level which significantly improves the mechanical properties of numerous materials.[1-3] Its leads to an increase in their strength and plasticity in a wide temperature range.[3-10] The most common among the methods of SPD are high- pressure torsion (HPT), proposed at the beginning of the twentieth century by W. Bridgman,[4, 11] the method of equal-channel angular pressing (ECAP) actively developed since the 1990s[3, 5] and modifications of these methods. At the same time, SPD deformation and large deformations by rolling carried out at ambient temperature has a number of limitations. At large deformations (e ~ 8-10), the process of grain refinement becomes more difficult due to the increased influence of dynamic processes of structure recovery.[11, 12] In addition SPD materials have insufficiently high thermal stability[13] and their use at elevated temperatures, and sometimes even at room temperature, may have significant limitations. Reducing the temperatures of SPD and rolling to 77 K leads to an improvement in the mechanical properties, in particular an increase in the yield strength and tensile strength) of many deformable materials.[7, 14-21]

Currently, there are a large number of reviews on the mechanical properties of SPD metals and their alloys.[2, 3, 11, 12, 22-72] However, at present, the number of reviews devoted to the effect of SPD at cryogenic temperatures (cryo-SPT) and cryorolling on the mechanical properties of metallic materials at low temperatures is very limited. Therefore, the purpose of this review is to discuss the results of studies of low-temperature mechanical properties of metallic materials in the temperature range of 4.2 -300 K after cryo-SPD and cryo-rolling using data obtained mainly by the authors of this review. The results of the effect of cryo-SPD on low-temperature mechanical properties and deformation

mechanisms in various materials (titanium and its alloys, cobalt, zirconium, high-entropy alloys of various compositions, Ni-18.75 at.% Fe alloy) are discussed. In addition, there are currently no review articles on the mechanical properties of metallic materials in different structural states in the ultralow temperature range (0.5-4.2 K). Therefore, this article includes the results of studies on the mechanical properties of some ultrafine-grained (UFG) and nanostructured (NS) metals and alloys obtained both by cryo-SPD and SPD at 300 K.

Section 2 describes the effect of temperature during SPD and rolling on the low-temperature mechanical properties and microstructures of various materials. Section 3 presents data on the mechanisms of plastic deformation obtained using the method of thermal activation analysis of this process. Section 4 for the ultralow temperature range (0.5-4.2 K) presents data on the mechanical properties of some UFG and NS metals and alloys obtained after SPD at 300 K and 77 K.

2. Mechanical properties of ultrafine-grained and nanostructured metals and alloys produced by cryo-SPD and cryo-rolling

Nanostructured (NS) and ultrafine-grained (UG) metals and alloys produced by cryo-SPD and cryo-rolling exhibit exceptional mechanical properties over a wide temperature range, especially at cryogenic temperatures, due to the activation of additional deformation mechanisms such as twinning and phase transitions.[73-87)] The coexistence of multiple deformation paths obviously influences the evolution of the microstructure during deformation and the individual competing or interacting deformation mechanisms during cryo-SPD and cryo-rolling. This chapter discusses the research[14-16, 87-103)], carried out mainly by the authors of this review, on the effect of different cryo-SPD methods (cryo-rolling, equal channel-angular pressing (ECAP), quasi-hydroextrusion, high-pressure torsion (HPT)) on the mechanical properties of some metals (titanium , zirconium, cobalt), Ni-18.75 at.% Fe alloy and a number of high-entropy alloys (HEAs).

2.1. Cryo-SPD and cryo-rolling in titanium Grade 2

The successful technical use of titanium and its alloys as structural materials is due to their high specific strength and high plasticity in a wide temperature range up to cryogenic temperatures on account of the specific deformation mechanism of titanium.[104-106)] As shown in several reports[98, 99, 107-112)], in ultrafine-grained titanium and its alloys processed by ECAP at 300 K when the deformation temperature is lowered to 4.2 K high strength and ductility are observed. To improve the mechanical properties of titanium, both the cryo-SPD and cryo-rolling methods have been used.[7, 16, 100-103)] Note that the structure of titanium, in contrast to the structure of niobium,[2)] has a high thermal stability after cryo-rolling.

2.1.1. Cryo-rolling of commercial-pure titanium (CP-Ti) Grade 2

One of the most prevalent methods of large deformations is the cryo-rolling method.[100-103, 113-116)] These works studied in detail the regularities of microstructure formation during cryo-rolling and rolling at 300 K, as well as the temperature dependences of the mechanical characteristics of commercial-purity titanium (CP-Ti Grade 2). It turned out that the rolling temperature significantly affects the kinetics of the deformation process during rolling. It has been found that large degrees of rolling to a true thickness strain of 2.66[103)] led to the formation of a microstructure with a grain size of 80 nm or 200 nm at 77 K or 293 K, Fig. 1(a), (b). In this case the ultimate tensile strength reaches values of 1100 MPa or 900 MPa at 77 K or 293 K, respectively. An even smaller average grain size after cryorolling (40 nm) was obtained in other research[102)]. It is assumed that the nanosized grain excludes the possibility of mechanical twinning and, consequently, further grain fragmentation. The closeness of the average grain size to the crystallite size may indicate the perfect internal structure of

nanocrystalline titanium grains. This result confirms the idea of the impossibility of accumulation of dislocations in nanosized grains, which are the source of lattice distortions.[102, 103)]

It was concluded[103)] that the evolution of the microstructure of CP titanium during cryo-rolling in the range of 0.06–3 true strains and the nature of the change in the average grain size during cryo-deformation corresponds to the stages of mechanical twinning activity. The initial intense fragmentation of grains ($e \leq 0.3$) is associated with the appearance of twins of the first generation and the formation of a predominantly laminar twin structure. The second stage ($|e| \sim 0.3–1.2$) is primarily due to the activation of secondary (tertiary) twinning and corresponds to a decrease in grain size from submicron to nanoscale values (~100 nm). The third stage ($|e| \geq 1.3$) corresponds to a monomodal nanocrystalline state, when a further increase in cryo-deformation occurs without changing the average grain size. The limit of grain refinement during the processing of nanocrystalline titanium by the method of cryo-mechanical grain fragmentation is ~ 40 nm. In an earlier report[103)] it is shown that the active contribution of twinning processes to the overall deformation, observed at the initial stages of cryo-rolling, decreases when the size of grains / subgrains becomes comparable with the average thickness of twins or the distance between twin boundaries (Table 1). Inside the twins, new dislocations are formed that interact with each other,[117)] leading to high strain hardening.

The studies of the evolution of the microstructure carried out by the authors showed that, at the initial stages of cryo-rolling, high-angle boundaries are formed in the alloy structure as a result of twinning, leading to lattice reorientation. The increase in strain hardening is also affected by the slower, compared to rolling at 300 K, dynamic recovery process. These and other studies of the microstructure and mechanical properties of nanocrystalline titanium obtained by cryo-rolling suggest that titanium cryo-rolling is a reliable and efficient way to obtain high-strength titanium suitable for structural and functional applications.

2.1.2. Combination of different deformation methods: equal-channel angular pressing and quasi-hydroextrusion

An interesting result was also obtained[104)] where polycrystalline Ti Grade2 was subjected to deformation by various SPD methods: equal-channel angular pressing (8 passes at 720 K) and quasi-hydroextrusion to different degrees of deformation at different temperatures (300 and 77 K).

As a result of applying a combination of different methods in the studied Ti Grade 2, various sets of effective slip and twinning systems were realized during plastic deformation, which significantly affected its microstructure and mechanical properties. Eight different structural states were obtained, for which the following parameters were measured: average grain size, microhardness values (at 300 K) and mechanical characteristics under uniaxial compression with an initial strain rate of 4×10^{-4} s^{-1} at temperatures of 300, 77 and 4.2 K. It turned out that the minimum average grain size, the maximum value of microhardness and the yield strength and strength are observed when sequentially using simple shear deformation (using ECAP at 300 K samples) and axisymmetric deformation at 77 K (using cryoquasi-hydroextrusion samples) in the course of deformation. This nanocrystalline state corresponds to an average minimum grain size of the order of 0.1 μm (Fig.2) and maximum values of mechanical characteristics at all test temperatures.

Thus, it was shown[104)] that cryoquasi-hydroextrusion, in combination with other SPD methods, makes it possible to implement a set of effective sliding systems, the action of which leads to the achievement of optimal mechanical properties in Ti Grade 2 at temperatures of 300, 77 and 4.2 K.

2.1.3. Cryo-ECAP of titanium

In recent decades, to improve the mechanical properties of titanium, one of the SPD methods has been used - the ECAP method, usually used at 300 K and elevated temperatures.[7, 118-120, 121)] Cryo-SPD by ECAP of commercially pure titanium (CP-Ti) Grade 2 (0.16 wt% O) has been carried out for the first time in this work.[7)] Samples of 35 mm length were cut from the rod and dipped into liquid nitrogen. Then, the samples were dropped in the entry channel of an ECAP rig and immediately pressed. The time between extracting the sample from liquid nitrogen and the end of pressing did not exceed 10 s. It should be noted previous experimental studies of thermal diffusivity of CP-Ti[122)] and numerical simulations of temperature during ECAP show that this time is insignificant to change the temperature within the sample, except in the very thin surface layers which are removed before microstructural or mechanical study. At a temperature of 77 K, the samples were deformed by one, two and three passes of ECAP. The microstructure and mechanical properties studied after cryo-ECAP are compared with similar patterns obtained at 300 K and 575 K (Fig. 3). It turned out that the microstructure formed during cryo-ECAP significantly depends on the number of passes during cryo-ECAP. During the 1st and 2nd pass, both areas of ultrafine grains (of the order of microns) and larger grains coexist in the structure. After three passes of cryo-ECAP, a more uniform microstructure with smaller average grain sizes is formed than after a similar deformation at 300 and 575 K. The crushing of grains to average sizes d of the order of microns is responsible, according to the Hall-Petch ratio $\sigma_{0.2} = \sigma_0 + kd^{-1/2}$, for increasing the strength characteristics of the alloy. After cryo-ECAP in the temperature range from 300 to 4.2 K, the yield strength at uniaxial compression deformation (at a rate of $3\ 10^{-4}\ s^{-1}$) is approximately 5–10% higher than the corresponding values after ECAP at 300 K. This makes it possible to characterize cryo-ECAP as one of the ways to increase the strength of the material in a wide temperature range down to cryogenic temperatures while maintaining a sufficiently high plasticity.

2.2. Influence of cryo-HPT on the microstructure and mechanical properties of various materials: metals and HEAs

In reports[14-16], for a number of metals (ultrapure titanium, commercially pure zirconium and cobalt), a nanostructural high-strength state was obtained using HPT at 300 and 77 K. This method, widely is used for fundamental research,[96, 123-129] and it allows grains refined to NS for a wide class of materials due to the unique combination of high compressive hydrostatic stresses and continuous shear by torsion in HPT. [17-20, 130-133] Obviously, a decrease of the deformation temperature during HPT from 300 K up to 77 K improves the mechanical properties of many metallic materials due to the slowdown in the dynamic recovery of the structure during deformation at low temperatures, as well as the action of twinning as an additional deformation mechanism.

2.2.1. Influence of cryo-HPT on the microstructure and mechanical properties of some metals (titanium, cobalt and zirconium)

It was shown earlier[14-16, 81] that lowering the HPT temperature from 300 K to 77 K leads to a decrease in the average grain size and an improvement in the mechanical characteristics. For example, there is a report[16] that in polycrystalline high purity Ti (the total impurity content was about 0.01 wt%) after cryo-deformation the formation of finer grains (of the order of 100 nm) is observed by comparison with the average grain size after HPT at 300 K (of the order of 160 nm) as well as an increase in the density of accumulated dislocations including twins.

It has been shown that cryo-HPT significantly improves both the microhardness (Table 2) and the mechanical characteristics of titanium during uniaxial compression at a rate of 4×10^{-4} s^{-1} at temperatures of 300, 77 and 4.2 K (Fig. 4). It can be seen from the given parameters that the yield strength in polycrystalline high purity Ti (after cryo-HPT) under uniaxial compression reaches

1.4 GPa, which is almost 5 times higher than in coarse-grained (CG) titanium and 10% higher than after HPT at 300 K. Note that in the nanostructured state, in contrast to the coarse-grained state, there is no significant effect of titanium purity on its strength.

The authors[14, 15)] also studied the effect of cryo-SPD on the microstructure and mechanical properties of zirconium and cobalt polycrystals, in which after cryo-HPT the highest values of microhardness and mechanical characteristics were also found. An earlier report[14)] described polycrystalline zirconium with an average grain size of 10 μm, and a total impurity content of about 0.2 wt.%, subjected to HPT deformation up to shear strain $\gamma \approx 200$ at pressures of 2 and 4 GPa at temperatures of 300 and 77 K with different modes of subsequent annealing. It turned out that HPT processing at cryogenic temperature of 77 K (pressure of 2 GP) produces a very fine-grained and uniform microstructure of zirconium with an average grain size of 80 nm. This value is much smaller than the final grain sizes after HTP at 300 K (around 200 nm).

This structural state corresponds to the maximum values of mechanical characteristics upon deformation by uniaxial compression at a rate of 5×10^{-4} s^{-1} at temperatures of 300 K, 77 K and 4.2 K (Fig. 5).

An improvement in the mechanical properties after cryo-HPT was also found for nanostructured polycrystalline cobalt[15)] where the mechanical properties of nanostructured Co were studied by microhardness measurements at 300 K, and uniaxial compression at temperatures of 300, 77 and 4.2 K. Several nanostructured states of high purity cobalt were achieved by HPT at pressures of 4 and 8 GPa and temperatures of 300 K and 77 K. It is shown that cryogenic HPT at 77 K allows smaller grain sizes (70 nm), while in the structure obtained after HPT at 300 K the average grain size is about 100 nm. A decrease of the grain size down to 70 nm after cryo-HPT leads to an additional increase of 10% in strength at all studied temperatures. In addition, strength at a temperature of 77 K after cryo-HPT and annealed structural states is 15-20 % higher in comparison

with the non-annealed states. This effect may be explained by the different level/distribution of internal stress in as-HPT processed and additionally annealed samples.

2.2.2. Influence of cryo-HPT on the microstructure and mechanical properties of several HEAs

The cryo-HPT method was used to obtain a nanostructural state in a new class of materials - multicomponent alloys, called high-entropy alloys (HEAs) - and this makes it possible to obtain a microstructure with an average grain size of about 100 nm.[78, 79, 87, 93)] It has been established[6)] that after cryo-HPT in the temperature range of 350–4.2 K in one of the most studied HEA CoCrFeNiMn (in the so-called Cantor alloy) in the nanostructured state, there is a strong temperature dependence of the yield strength $\sigma_{0.2}$ (1.44 GPa and 2.48 GPa at 350 K and 4.2 K, respectively) while maintaining high plasticity (Fig. 6.). Such a strong temperature dependence of the yield strength $\sigma_{0.2}$ indicates the thermally-activated nature of the plastic deformation process in this temperature range. However, some HEAs (CoCrFeNiMn, $CoCrFeNiMnV_{0.2}$, $Co_{20}Cr_{26}Fe_{20}Mn_{20}Ni_{14}$)[78, 79, 87, 93, 96)] after cryo-HPT showed a contrary result - lower values of the yield strength (Fig. 6), deforming stress and microhardness (Figs. 7, 8) characteristics after cryo-HPT than with HPT processing at T = 300 K, which is inconsistent with these ideas. Note that a similar decrease in strength characteristics in materials treated with cryo-HPT was observed in some metals[70, 134-136)]. Such softening after cryo-HPT, called “self-annealing,” was associated with a static recrystallization process to reduce the high stored energy caused by cryo-HPT. In the $Co_{20}Cr_{26}Fe_{20}Mn_{20}Ni_{14}$ alloy, similar self-annealing effects can appear due to the minimum stacking fault energy (SFE) equal to (3.5 mJ/m^2) (in the NiFeCrCoMn system)[137)] due to the accumulation of the maximum stored strain energy in the sample during cryo-HPT. The results on microstructure and dislocation density evolution driven by the tendency of the $Co_{20}Cr_{26}Fe_{20}Mn_{20}Ni_{14}$ alloy to accommodate the stored strain energy during and

after cryo-HPT are summarized schematically in Fig. 9. At the same time, a similar behavior was also observed after cryo-preservation in CoCrFeMnNi and $CoCrFeNiMnV_{0.2}$ HEAs with a higher SFE. To explain this unusual phenomenon, a comparative study[78, 79, 87, 93)] of the microstructure of alloys was carried out, depending on the temperature of the HPT. A number of features were found associated with differences in the formation of the microstructure during HTP at 300 K and 77 K. It was found that during HPT there is a phase transformation from the fcc to the hcp phase (Fig. 10) and an associated decrease in the dislocation density during cryo-HPT. In recent work[78)] it was shown that the volume fraction of the hcp phase increases with increasing HPT pressure. It was also found that in cryo-SPD nanostructured CoCrFeMnNi, exposure to time at room temperature can lead to a reverse transformation, the magnitude of which depends on the pressure and number of revolutions during cryo-SPD. Such an inverse transformation complicates the study of the discussed anomalous dependence and makes it possible to explain its absence[80)].

3. Thermally-activated deformation of nanocrystalline and coarse-grained metals and alloys in the temperature range 4.2–350 K

The problem of determining the physical mechanisms that control the low temperature plastic deformation of nanostructured metals and alloys, including HEAs, is widely discussed in the modern literature.[47, 48, 50, 138-140)] This section presents the results of studies[141-146)] with the mechanisms that control low-temperature plastic deformation, which were found using the method of thermal-activation analysis proposed elsewhere[147, 148)] and used extensively.[141-146, 149)] A brief description of this method is as follows. It is assumed that macroscopic plastic deformation, carried out by the movement of a large number of dislocations in many grains, is determined by the microscopic mechanism of thermally-activated breakaway of dislocations moving inside grains from local obstacles. The theoretical dependences of the deforming stress, rate sensitivity, and activation

volume of plastic deformation were obtained on the basis of the well-known classical Arrhenius relation,[117] which describes the dependences between the plastic deformation rate $\dot{\varepsilon} = d\varepsilon/dt$, effective stress τ^*, and temperature T:

$$\dot{\varepsilon} = \dot{\varepsilon}_0 \exp\left[-\frac{H(\tau^*)}{kT}\right] \tag{1}$$

where $\dot{\varepsilon}_0$ is a temperature-dependent pre-exponential factor, which is considered as a constant value in this method, $\tau^* = \tau - \tau_i$ is the effective stress, τ_i is the long-range internal stress; $H(\tau^*)$ is the effective energy (enthalpy) of activation which depends on the parameters of local barriers and statistical differences of these barriers on dislocations. In most cases,[117] the function $H(\tau^*)$ is well approximated by an analytical expression in the form:

$$H(\tau^*) = H_0\left[1-\left(\frac{\tau^*}{\tau_c}\right)^p\right]^q, \quad 0 \le p \le 1, \quad 1 \le q \le 2 \tag{2}$$

where H_0 is the energy parameter that ensures the interaction of the dislocation with the local barrier; τ_c is the critical stress of activation less overcoming of the local barrier; and p and q are numerical parameters where the value of q depends on the shape of the barrier and the parameter p depends on its properties and the statistics of barriers on dislocations. From relations (1) and (2), theoretical expressions (3) - (5) for the deforming stress and the speed sensitivity of the deforming stress are obtained:

$$\tau(T) = \tau_i + \tau_c\left[1-\left(\frac{T}{T_0}\right)^{\frac{1}{q}}\right]^{\frac{1}{p}} \tag{3}$$

$$\left(\frac{\partial \tau^*}{\partial \ln \dot{\varepsilon}}\right)_T = \frac{\tau_c}{pqA}\left(\frac{T}{T_0}\right)^{\frac{1}{q}}\left[1-\left(\frac{T}{T_0}\right)^{\frac{1}{q}}\right]^{\frac{1-p}{p}} \tag{4}$$

$$V(T) = -\left(\frac{\partial H}{\partial \tau^*}\right)_T = \frac{pqH_0}{\tau_c}\left(\frac{T}{T_0}\right)^{1-\frac{1}{q}}\left(1-\left(\frac{T}{T_0}\right)^{\frac{1}{q}}\right)^{\frac{p-1}{p}} \quad (5)$$

where $A = \ln(\dot{\varepsilon}_0/\dot{\varepsilon})$, $T_0 = H_0/kA$.

Parameters τ_c, τ_i and H_0 in relations (3)–(5) in the general case should depend on temperature T due to the temperature dependence of the elastic constants, however, in reports[141-146] these corrections are not taken into account in the limited temperature range (25 K ≤ T ≤ 350 K) in the analysis. Using the experimental dependences $\tau_2(T)$, (τ_2 is the value of τ at $\varepsilon \approx 2\%$), and in reports[141-146] empirical values of the parameter A were obtained for different temperatures

$$A = -T\left(\frac{\Delta\tau}{\Delta \ln \dot{\varepsilon}_a}\right)_T^{-1}\frac{d\tau_2}{dT} \quad (6)$$

The value of A within scatter in the temperature range 25 K ≤ T ≤ 350 K does not depend on temperature and its average value is 25.[141-146] The athermicity of the parameter A in this consideration confirms the validity of the assumption that the parameters τ_c, τ_i, and H_0 are independent of temperature, and also indicates the applicability of the assumption $\dot{\varepsilon}_0 = const$ in relation (1). Using the obtained theoretical and experimental temperature dependences (3)-(5) of the deforming stress, the velocity sensitivity of the deforming stress, and the activation volume of the thermally-activated movement of dislocations, they are compared by double approximation using the least squares method. The results experimentally obtained[141-146] are quite well described by theoretical dependences (Figs. 11, 12). This allows us to conclude that there is a single mechanism that controls thermally-activated plasticity in the studied materials and to determine the empirical parameters of the theory (values p, q, T_0, τ_c, τ_i given in Table 3). Based on the analysis of the obtained data, it is possible to obtain information about the most probable type of barriers, breakaway from which determines the thermally-activated dislocation glide. It follows from Table 3

that the parameter *p*, which characterizes the statistics of dislocation barriers, for all materials under study is equal to 2/3. This value corresponds to the Friedel statistics of the thermally-activated motion of dislocations through a network of randomly located local barriers.[117, 150, 151] Therefore, further analysis was conducted[141-146] and this made it possible to estimate the length of a dislocation segment bent under the action of a deforming stress between the pinning points and the density of pinning points on the dislocation line using the Friedel statistics[151] for various studied materials.

According to the analysis[151], the average length of a dislocation segment between two local barriers depends on the effective stress and is determined by the equation:

$$L(\tau^*) = \left(\frac{2E_d S_0}{b\tau^*} \right)^{\frac{1}{3}} \quad (7)$$

where E_d is the linear tension of the dislocation, S_0 is the average area per one local obstacle, and b is the magnitude of the Burgers vector. The value of S_0 can be estimated using the dependence for the activation volume in the form:

$$V = bwL \quad (8)$$

where $w = w(\tau^*)$ is the effective activation distance, which is due to the thermally-activated movement of dislocations through the system of local barriers.

$$S_0 = \frac{b^2\tau^*}{G}\left(\frac{b}{w}\right)^3\left(\frac{V}{b^3}\right)^3 \quad (9)$$

Numerical estimates are given [143-145] for HEAs in a coarse-grained state showing that the distance between local obstacles in the slip plane is l_0 =4.6 nm, which corresponds to the density of the assumed barriers, estimated as $1/S_0$, to a value of the order of 10^{17} m^{-2}. For forest dislocations, which, in principle, can be local barriers, this value at $\varepsilon \approx 2\%$ is unreasonably large. Assumptions about the controlling role of impurity atoms in this case are also unlikely, taking into account the value of the activation energy H_{00} = 0.65 eV (Table 3), which is characteristic of local obstacles

consisting of several atoms.[117] Therefore, in reports[143-145] it was concluded that in the temperature range $25\ \mathrm{K} \le T \le 300\ \mathrm{K}$, the most probable local barriers that control the process of plastic deformation can be several atoms (clusters) located at a distance of several nanometers. Clusters of this type were experimentally observed for coarse-grained HEA CrMnFeCoNi.[152]

In several reports[141, 142, 145] a difference was established in the physical mechanisms that control the thermally-activated motion of dislocations for the nanostructured and coarse-grained states. It was found[141, 149] that for NC and CG Ni-18.75 at.% Fe alloy, produced by electrodeposition, with an average grain size of $r \sim 23$ nm, and for CG Ni-Fe with an average grain size of $r \sim 35$ μm, the temperature dependences of the activation volume $V(\tau^*)$ obtained from equation (5) for the temperature range $23 \le T \le 350$ K do not match (Fig. 12). The difference in the empirical values of the parameters H_{00} and q given in Table 3 for these states and in the values of $1/S_0$, which is equal to 10^{19} m^{-2} for the nanostructured state, was also established. Based on the analysis of these results, it was shown[142] that in the Ni-18.75 at.% Fe alloy in the NC state, the most likely controlling mechanism is the breakaway of dislocations from the pinning points at the grain boundaries, while in CG materials, for slipping dislocations inside the grains, the controlling feature is their breakaway from local obstacles in the form of clusters of several atoms.

The thermal-activation analysis performed elsewhere[146] for CG (grain size $r = 2$ μm) and NC ($r = 35$ nm 45 nm) titanium VT1-0, obtained by cryo-mechanical grain fragmentation, deformed by uniaxial tension in the temperature range 4.2–395 K, showed that the process of plastic deformation under conditions of ambient and low temperatures is determined by the overcoming of local impurity barriers by dislocations, where the grain boundaries are a source of internal stresses. Empirical estimates were obtained for the parameters of the dislocation-impurity interaction. The unambiguous relationship between internal stresses and grain size established for monomodal nanocrystalline titanium made it possible to separate the effects of impurity and grain boundary

hardening. The result obtained is an indirect basis for the conclusion about the impossibility of an accumulation of dislocations in nanograins during plastic deformation. The decrease in the activation volume for a nanoscale grain at a constant impurity concentration is considered because of the manifestation of the dependence of the diameter of the dislocation loop generated by a grain boundary source on the grain size (confinement effect).

Thus, as shown earlier[141-146] the use of the thermal-activation analysis method makes it possible to establish the most probable physical mechanisms that determine the plasticity of a wide class of materials. It is obvious that for a more accurate comparison of the results of theory with experiment, it is necessary to carry out detailed microstructural studies in the future to confirm these findings.

4. Mechanical properties of some coarse-grained and ultrafine-grained metals and alloys in the ultralow temperature range (0.5-4.2 K)

Studies of the mechanical properties of a number of metals and alloys at ultralow temperatures (0.5-4.2 K) started in 2006 and are published in numerous reports[153-164]. The studies carried out in the field of ultralow temperatures became possible due to the use of a unique deformation setup,[153, 165] in which the samples were cooled by evacuation of vapours of liquefied ^{3}He which at temperatures below 1 K has a higher cooling capacity compared to conventional ^{4}He. The difficulties of using ^{3}He in this temperature range are exacerbated by the requirement to minimize heat release from the sample during deformation and heat transfer through the grips of the testing machine to stabilize the temperature of the experiment. In this regard, the results of the experimental studies presented in this section are pioneering and unique.

In the region of ultralow temperatures, one can expect a manifestation of specific dynamic and quantum properties of dislocations during their motion in the course of plastic deformation and related features in mechanical properties. Obviously, the study of the physical and mechanical properties of metals and alloys at ultralow temperatures (0.5-4.2 K) is relevant both for their practical application and for establishing the fundamental physical mechanisms of plastic deformation.

One of the most characteristic features currently found experimentally for a number of metals and alloys[153, 160-164)] in the region of ultralow temperatures is the inverse (anomalous) temperature dependence of the yield strength. Such an anomalous dependence was observed in ultrafine-grained (UFG) copper in different structural states,[153)] as well as in a number of HEAs including coarse-grained $Al_{0.5}CoCrCuFeNi$,[160)] $Co_{17.5}Cr_{12.5}Fe_{55}Ni_{10}Mo_5$,[161, 164)] $Fe_{40}Mn_{40}Co_{10}Cr_{10}$ (Twinning Induced Plasticity - TWIP) and $Fe_{50}Mn_{30}Co_{10}Cr_{10}$ (Transformation-Induced Plasticity - TRIP)[162-164)] (Fig. 13, 14, Table 4). The observed anomalous temperature dependence of the yield strength contradicts the laws of thermally-activated plastic deformation established for these materials in the higher temperature range, where the yield strength (σ_0) increases monotonically with decreasing temperature.[166-169)] In earlier reports,[167-169)] the anomalous behaviour of $\sigma_0(T)$ is explained by the change in the mechanism of dislocation motion through local barriers from thermally-activated to inertial. Under these conditions, the contribution of thermal activation to the process of overcoming obstacles by moving dislocations decreases. Below a certain temperature T_c, the viscous drag of dislocations as they move between local obstacles becomes low due to a significant drop in its phonon component, which leads to an anomalous nature of the temperature dependence of the yield strength. It should be noted that in the range of ultralow temperatures down to 0.5 K, the studied materials remain plastic and in some cases (in UFG copper in some structural states and in

HEA $Fe_{50}Mn_{30}Co_{10}Cr_{10}$) an increase in plasticity is observed with decreasing temperature to 0.5 K (Table 4).

The second typical feature of plastic deformation processes in the range of 0.5-4.2 K for the studied materials is the unstable (jump-like) nature of plastic deformation - LTSD (low-temperature serrated deformation).[153-164] It is known that for many metals and alloys stress jumps appear on deformation curves at temperatures of the order of 15 K and reflect the localization of slip during deformation.[170] The "classical" dislocation theories of LTSD are based on the concept that stress jumps on the deformation curve are the result of the displacement of a critical number of closely connected dislocation segments (dislocation avalanches) due to their detachment or destruction (collapse) of barriers under the action of external stress and thermal fluctuations. The parameters of jumps on the deformation curve depend on many factors: temperature, strain rate, deforming stress, and grain size.[170-175] In the ultralow temperature range of 0.5-4.2 K, the LTSD parameters (amplitude, frequency, and other characteristics) also strongly depend on these factors. Possible causes and mechanisms of LTSD at extremely low temperatures[153-164] are associated with the following where it is sufficient to activate the processes of dynamic recovery as a result of which the coefficient of strain hardening decreases. An increase in the characteristic scale of LTSD compared to coarse-grained copper at low temperatures is determined by evidence for the inertial properties of dislocations,[172] which manifest themselves under conditions of low phonon friction and high effective stresses.[173] For UFG copper of 99.95% purity,[153] the relationship between the scale of instability at LTSD and the grain size and strain hardening rate was found. In the UFG alloy Al-3.8 at.% Li, with a microstructure obtained as a result of SPD by the hydro-extrusion method,[156] it was found that the nature of LTSD is associated with the processes of evolution of the dislocation density. The amplitudes of stress jumps during LTSD were considered as random events associated with the scale of dislocation avalanches, leading to a local shift of the crystal cell. For the Al-3Mg

alloy,[156] the observed frequency of stress jumps on the deformation curves increases with decreasing temperature from 4.2 to 0.5 K. It is important to note that the jumps observed at 300 K, caused by the action of the Portevin-Le Chatelier effect, differ in their parameters from the jumps at low temperatures. In UFG magnesium alloys AE42 (4.0% Al, 2.0% Rare Earth elements (RE), 0.2% Mn) and AZ31 (3.1% Al, 0.8% Zn, and 0.2% Mn, all in wt%) at temperatures of 4.2 K and below, the amplitude and frequency of stress jumps on the deformation curves at LTSD increases with an increase in the flow stress and a decrease in temperature. The microstructure of the alloys was characterized in two ways: for AE-42 a bimodal distribution with grain sizes of 3–4 μm and 1 μm, respectively, and for AZ31 the grain size was 2–3 μm. The presence of LTSD in the ultralow temperature range of 0.5-4.2 K is also characteristic of a new class of materials - HEA (Fig.13).[160-164] In HEA, the amplitude and frequency of LTSD surges depends on temperature and strain such that, as the temperature decreases and the degree of strain increases, LTSD increases. Based on the obtained experimental data, it is assumed that the low-temperature jump-like deformation in HEAs has the same nature as in conventional fcc alloys.[170-175]

5. Summary and conclusions

In this article, using the example of a wide class of materials: pure metals, traditional and high-entropy alloys, the following results are demonstrated:

1. Lowering the sever plastic deformation temperature from 300 to 77 K (cryo-SPD) is an effective method to improve the mechanical properties (yield strength, tensile strength, microhardness value). It has been established that the increase of mechanical characteristics in materials of a wide class after cryo-SPD is approximately 10% compared with similar values after SPD at 300 K. In cryo-high-pressure torsion processed polycrystalline high purity Ti the

yield strength under uniaxial compression reaches 1.4 GPa at 4.2 K, which is almost 5 times higher than in coarse-grained titanium and 10% higher than after high-pressure torsion at 300 K. In high-entropy alloys CoCrFeNiMn after cryo-SPD under uniaxial compression in the entire temperature range of 4.2-300 K, a record high strength is achieved (~ 3 GPa at 4.2 K). Thus, the totality of the results presented in the article on the mechanical properties of nanostructured metals and alloys produced by cryo-SPD shows that this method is a reliable way to obtain materials having the attractive properties required for functional and structural applications.

2. It is shown that the application of the method of thermal activation analysis makes it possible to establish the most probable physical mechanisms that determine the plasticity of a wide class of materials. It was found that in nanostructured titanium VT1-0 obtained by cryomechanical grain fragmentation, the most likely mechanism controlling the process of thermally-activated deformation during uniaxial tension in the temperature range 4.2–395 K is the overcoming of dislocations from local impurities. For nanostructured and coarse-grained high-entropy alloys CoCrFeNiMn, CG $Al_{0.5}$CoCrCuFeNi, CG CrMnFeCoNi_2Cu, CG Ni-18.75 at.% Fe alloy, such a mechanism is overcoming the dislocations of a set of several atoms (clusters) located at a distance of several nanometers from each other. At the same time, in the nanostructured state for the Ni-18.75 at.% Fe alloy, the most probable controlling mechanism is the overcoming of the pinning points at the grain boundaries by dislocations.

3. For high-entropy alloys (CoCrFeNiMn, CoCrFeNiMn$V_{0.2}$, $Co_{20}Cr_{26}Fe_{20}Mn_{20}Ni_{14}$), an unusual result was found with lower values of the yield strength, deforming stress and microhardness characteristics after cryo-high-pressure torsion than with a similar treatment at T = 300 K, where this result does not correspond to current ideas on the thermally activated nature of plastic deformation. It has been established that this phenomenon is associated with

low temperature fcc-hcp phase transformations initiated by plastic deformation during high-pressure torsion at 77 K. Such transformations lead to changes in in the microstructure such as high inhomogeneity, an increase in the average grain size and a decrease in the average dislocation density. The study of the features of the high-entropy alloys microstructure that arise during high- pressure torsion makes it possible to simulate their mechanical behavior, and this is necessary to obtain materials with desired properties.

4. It is shown that the study of the physical and mechanical properties of metals and alloys at ultralow temperatures (0.5-4.2 K) is relevant both for their practical application and for establishing the basic physical mechanisms of plastic deformation. Among the low-temperature features found in ultrafine-grained and nanostructured Cu, in coarse-grained high-entropy alloys $Al_{0.5}CoCrCuFeNi$, $Co_{17.5}Cr_{12.5}Fe_{55}Ni_{10}Mo_5$, $Fe_{40}Mn_{40}Co_{10}Cr_{10}$ and $Fe_{50}Mn_{30}Co_{10}Cr_{10}$, the most characteristic are: 1) an inverse (anomalous) temperature dependence of the yield strength, which contradicts the regularities of thermally activated plastic deformation characteristic of these materials in the higher temperature range: this phenomenon is explained by a change in the rate-controlling mechanism of dislocation movement through local barriers from thermally-activated to inertial; 2) a change in the nature of plastic flow from smooth to abrupt. This phenomenon of low temperature serrated deformation reflects the localization of slip during deformation, the causes of which require further experimental and theoretical studies.

Acknowledgements

The authors gratefully acknowledge helpful discussions with Dr Michail Tikhonovsky, Dr Serhii Smirnov and Dr Aleksey Podolskiy. Two authors (YH and TGL) were supported by the European Research Council under ERC Grant Agreement No. 267464-SPDMETALS.

References

1. R.Z. Valiev, A.P. Zhilyaev and T.G. Langdon: *Bulk Nanostructured Materials: Fundamentals and Applications*, (Wiley Hoboken, NJ USA, 2014) pp. 456.
2. K. Edalati, A. Bachmaier, V.A. Beloshenko, Y. Beygelzimer, V.D. Blank, W.J. Botta, K. Bryła, J. Čížek, S. Divinski, N.A. Enikeev, Y. Estrin, G. Faraji, R.B. Figueiredo, M. Fuji, T. Furuta, T. Grosdidier, J. Gubicza, A. Hohenwarter, Z. Horita, J. Huot, Y. Ikoma, M. Janeček, M. Kawasaki, P. Král, S. Kuramoto, T.G. Langdon, D.R. Leiva, V.I. Levitas, A. Mazilkin, M. Mito, H. Miyamoto, T. Nishizaki, R. Pippan, V.V. Popov, E.N. Popova, G. Purcek, O. Renk, Á. Révész, X. Sauvage, V. Sklenicka, W. Skrotzki, B.B. Straumal, S. Suwas, L.S. Toth, N. Tsuji, R.Z. Valiev, G. Wilde, M.J. Zehetbauer and X. Zhu: Mater. Res. Lett. **10** (2022) 163–256.
3. R.Z. Valiev, R.K. Islamgaliev and I.V. Alexandrov: Prog. Mater. Sci. **45** (2000) 103–189.
4. P.W. Bridgman: Phys. Rev. **48** (1935) 825–847.
5. R.Z. Valiev, O.A. Kaibyshev, R.I. Kuznetsov, R.S. Musalimov and N.K. Tsenev: Dokl. Akad. Nauk SSSR **301** (1988) 864–866.
6. R.Z. Valiev, Y. Estrin, Z. Horita, T.G. Langdon, M.J. Zehetbauer and Y.T. Zhu: JOM **58** (2006) 33–39.
7. A.V. Podolskiy, H.P. Ng, I.A. Psaruk, E.D. Tabachnikova and R. Lapovok: J. Mater. Sci. **49** (2014) 6803–6812.
8. J.W. Yeh, S.K. Chen, S.J. Lin, J.Y. Gan, T.S. Chin, T.T. Shun, C.H. Tsau and S.Y. Chang: Adv. Eng. Mater. **6** (2004) 299-303.
9. B. Cantor, I.T.H. Chang, P. Knight and A.J.B. Vincent: Mater. Sci. Eng. A **213** (2004) 375–377.

10. D.A. Porter and K.E. Easterling: *Phase Transformations in Metals and Alloys*, (Chapman & Hall, London, 1992) pp. 514.

11. P.W. Bridgman: *Studies in large plastic flow and fracture*, (McGraw-Hill, New York (NY), 1952) pp. 362.

12. I.A. Ovid'ko, R.Z. Valiev and Y.T. Zhu: Prog. Mater. Sci.**94** (2018) 462-540.

13. R.A. Andrievski: J. Mater. Sci. **49** (2014) 1449-1460.

14. A.V. Podolskiy, E.D. Tabachnikova, B. Bonarski, D. Setman, C. Mangler, E. Schafler and M.J. Zehetbauer: Kovove Mater. **54** (2016) 1–8.

15. A.V. Podolskiy, D. Geist, E. Schafler, E.D. Tabachnikova and M.J. Zehetbauer: IOP Conf. Series: Mater. Sci. Eng. **63** (2014) 012103.

16. A.V. Podolskiy, C. Mangler, E. Schafler, E.D. Tabachnikova and M.J. Zehetbauer: Mater. Sci. **48** (2013) 4689–4697.

17. A. Bachmaier, M. Hafok and R. Pippan: Mater. Trans. **51** (2010) 8-13.

18. V.V. Popov, E.N. Popova, A.V. Stolbovskiy and V.P. Pilyugin: Mater. Sci. Eng. **A** 528 (2011) 1491-1496.

19. R. Vafaei, M.R. Toroghinejad and R. Pippan: Mater. Sci. Eng. **A536** (2012) 73-81.

20. V.V. Popov, E.N. Popova, D.D. Kuznetsov, A.V. Stolbovskii and V.P. Pilyugin: Phys. Met. Metallogr. **115** (2014) 682-691.

21. K. Edalati, I. Fujita, X. Sauvage, M. Arita and Z. Horita: J. Alloys Compd. **779** (2019) 394-398.

22. H. Gleiter: Acta Mater. **48** (2000) 1-29.

23. K.S. Kumar, H. Van Swygenhoven and S. Suresh: Acta Mater. **51** (2003) 5743-5774.

24. R.Z. Valiev: Nature Mater. **3** (2004) 511-516.

25. I.A. Ovid'ko: Int. Mater. Rev. **50** (2005) 65-82.

26. D. Wolf, V. Yamakov, S.R. Phillpot, A. Mukherjee and H. Gleiter: Acta Mater. **53** (2005) 1-40.

27. M.A. Meyers, A. Mishra and D.J. Benson: Prog. Mater. Sci. 51 (2006) 427-556.

28. C.C. Koch: J. Mater. Sci. **42** (2007) 1403-1414.

29. M. Dao, L. Lu, R.J. Asaro, J.T.M. De Hosson and E. Ma: Acta Mater. **55** (2007) 4041-4065.

30. C.S. Pande and K.P. Cooper: Prog. Mater. Sci. **54** (2009) 689-706.

31. E.C. Aifantis: Mater. Sci. Eng. A **503** (2009) 190-197.

32. J.R. Greer and J.T.M. De Hosson: Prog. Mater. Sci. **56** (2011) 654-724.

33. Y.T. Zhu, X.Z. Liao and X.L. Wu: Prog. Mater. Sci. **57** (2012) 1-62.

34. R.Z. Valiev, I. Sabirov, A.P. Zhilyaev and T.G. Langdon: JOM **64** (2012) 1134-1142.

35. L. Mishnaevsky, E. Levashov, R.Z. Valiev, J. Segurado, I. Sabirov, N. Enikeev, S. Prokoshkin, A.V. Solov'yov, A. Korotitskiy, E. Gutmanas, I. Gotman, E. Rabkin, S. Psakh'e, L. Dluhoš, M. Seefeldt, A. Smolin: Mater. Sci. Eng. R **81** (2014) 1-19.

36. M.E. McHenry, M.A. Willard and D.E. Laughlin: Prog. Mater. Sci. **44** (1999) 291-433.

37. M.H. Phan and H.X. Peng: Prog. Mater. Sci. **53** (2008) 323-420.

38. Y.Q. Chang, Q. Guo, J. Zhang, L. Chen, Y. Long and F.R. Wan: Front. Mater. Sci. **7** (2013) 143-155.

39. C.N.R. Rao, A. Müller and A.K. Cheetham: *The Chemistry of Nanomaterials: Synthesis, Properties and Applications*, (Weinhein, Wiley, 2004) pp. 761.

40. C.C. Koch, I.A. Ovid'ko, S. Seal and S. Veprek: *Structural Nanocrystalline Materials: Fundamentals and Applications,* (Cambridge University Press, Cambridge, 2007) pp. 364.

41. M.J. Zehetbauer and Y.T. Zhu: *Bulk Nanostructured Materials*, (Wiley, Weinheim Germany, 2009) pp. 710.

42. S.C. Tjong: *Nanocrystalline Materials. Their Synthesis-Structure-Property Relationships and Applications*, (Elsevier, Amsterdam, 2013) pp. 418.

43. Y.M. Wang and E. Ma: Acta Mater. **52** (2004) 1699-1709.

44. I.A. Ovid'ko: Rev. Adv. Mater. Sci. **10** (2005) 89-104.

45. E. Ma: JOM **58** (2006) 49-53.

46. I.A. Ovid'ko and T.G. Langdon: Rev. Adv. Mater. Sci. **30** (2012) 103-111.

47. R.Z. Valiev and Y.T. Zhu: Trans. MRS Japan **40** (2015) 309-318.

48. Y.H. Zhao, Y.T. Zhu and E.J. Lavernia: Adv. Eng. Mater. **12** (2010) 769-778.

49. R.Z. Valiev, Y. Estrin, Z. Horita, T.G. Langdon, M.J. Zehetbauer and Y.T. Zhu: Mater. Res. Lett. **4** (2016) 1-21.

50. Y.H. Zhao, Y.Z. Guo, Q. Wei, A.M. Dangelewiez, Y.T. Zhu, T.G. Langdon, Y.Z. Zhou and E.J. Lavernia: Scripta Mater. **59** (2008) 627-630.

51. Y.H. Zhao, Y.Z. Guo, Q. Wei, T.D. Topping, A.M. Dangelewicz, Y.T. Zhu, T.G. Langdon and E.J. Lavernia: Mater. Sci. Eng. A **525** (2009) 68-77.

52. A.P. Sutton and R.W. Ballufi: *Interfaces in Crystalline Materials*, (Clarendon, Oxford, 1995) pp. 856.

53. K. Ikeda, K. Yamada, N. Takata, F. Yoshida, H. Nakashima and N. Tsuji: Mater. Trans. **49** (2008) 24-30.

54. J.Y. Huang, Y.T. Zhu, H. Jiang and T.C. Lowe: Acta. Mater. **49** (2001) 1497-1505.

55. S. Divinski, H. Rösner and G. Wilde: *Functional Nanostructured Materials – Microstructure, Thermodynamic Stability and Atomic Mobility*. In: G. Wilde, Ed.: *Frontiers of Nanoscience*, (Elsevier, 2009) pp. 1-50

56. Y.R. Kolobov, R.Z. Valiev, G.P. Grabovetskaya, A. Zhilyaev and E.F. Dudarev: *Grain boundary diffusion and properties of nanostructured materials*, (Cambridge International Science Publishing, 2007) pp. 250.

57. L. Priester and D.P. Yu: Mater. Sci. Eng. A **188** (1994) 113-119.

58. G. Palumbo and K.T. Aust: Mater. Sci. Eng. A **113** (1989) 139-147.

59. S. Sonal and J. Lee: Metals **11** (2021) 1980.

60. J.W. Yeh, Y.L. Chen, S.J. Lin and S.K. Chen: Mater. Sci. Forum **560** (2007) 1–9.

61. E.J. Pickering and N.G. Jones: Int. Mater. Rev. **61** (2016) 183–202.

62. Z. Lyu, C. Lee, S.Y. Wang, X. Fan, J.W. Yeh and P.K. Liaw: Metall. Mater. Trans. A Phys. Metall. Mater. Sci. **50** (2019) 1–28.

63. Z. Li and D. Raabe: JOM **69** (2017) 2099–2106.

64. Z. Li, S. Zhao, R.O. Ritchie and M.A. Meyers: Prog. Mater. Sci. **102** (2019) 296–345.

65. S. Praveen and H.S. Kim: Adv. Eng. Mater. **20** (2018) 1700645.

66. B. Cao, T. Yang, W. Liu and C.T. Liu: MRS Bull. **44** (2019) 854–859.

67. E.W. Huang, G.Y. Hung, S.Y. Lee, J. Jain, K.P. Chang, J.J. Chou, W.C. Yang and P.K. Liaw: Crystals **10**, (2020) 200.

68. A.S. Rogachev, Phys. Met. Metallogr. **121** (2020) 733–764.

69. T.G. Langdon: Acta Mater. **61** (2013) 7035–7059.

70. K. Edalati, J.M. Cubero-Sesin, A. Alhamidi, I.F. Mohamed and Z. Horita: Mater. Sci. Eng. **A613** (2014) 103-110.

71. K. Edalati, Y. Hashiguchi, H. Iwaoka, H. Matsunaga, R.Z. Valiev and Z. Horita: Mater. Sci. Eng. **A729** (2018) 340-348.

72. V.V. Popov and E.N. Popova: Mater. Trans. **60** (2019) 1209-1220.

73. Y. Tong, D. Chen, B. Han, J. Wang, R. Feng, T. Yang, C. Zhao, Y.L. Zhao, W. Guo, Y. Shimizu, C.T. Liu, P.K. Liaw, K. Inoue, Y. Nagai, A. Hu and J.J. Kai: Acta Mater. **165** (2019) 228–240.

74. B. Gludovatz, A. Hohenwarter, D. Catoor, E,H. Chang, E.P. George and R.O. Ritchie: Science **345** (2014) 1153–1158.

75. Z. Li, K.G. Pradeep, Y. Deng, D. Raabe and C.C. Tasan: Nature **534** (2016) 227–230.

76. J.W. Bae, J.B. Seol, J. Moon, S.S. Sohn, M.J. Jang, H.Y. Um, B.-J. Lee and H.S. Kim: Acta Mater. **161** (2018) 388–399.

77. B. Gludovatz, A. Hohenwarter, K.V.S. Thurston, H.B. Bei, Z.G. Wu, E.P. George and R.O. Ritchie: Nat. Commun. **7** (2016) 10602.

78. R. Chulist, A. Pukenas, P. Chekhonin, A. Hohenwarter, R. Pippan, N. Schell and W. Skrotzki: Materials **15 (**2022) 8407.

79. A.V. Podolskiy, Y.O. Shapovalov, E.D. Tabachnikova, A.S. Tortika, M.A. Tikhonovsky, B. Joni, E. Ódor, T. Ungar, S. Maier, C. Rentenberger, M.J. Zehetbauer and E. Schafler: Adv. Eng. Mater. **22** (2020) 1900752 1 – 8.

80. Y. Ivanisenko, A. Kilmametov, H. Rösner and R.Z. Valiev: Int. J. Mater. Res. **99** (2008) 36–41.

81. K. Edalati, T. Daio, M. Arita, S. Lee, Z. Horita, A. Togo and I. Tanaka: Acta Mater. **68** (2014) 207–213.

82. H. Chen, V. Levitas and L. Xiong: Comput. Mater. Sci. **157** (2019) 132–135.

83. V.D. Blank and E.I. Estrin: *Phase transitions in solids under high pressure*, (CRC Press, New York, 2014) pp. 441.

84. N.V. Novikov, S.B. Polotnyak, L.K. Shvedov and V.I. Levitas: J. Superhard Mater. **21** (1999) 36–48.

85. K.K. Pandey and V.I. Levitas: J. Appl. Phys. **129** (2021) 115901.

86. K.K. Pandey and V.I. Levitas: Acta Mater. **196** (2020) 338–346.

87. J. Moon, Y. Qi, E. Tabachnikova, Yu. Estrin, W.-M. Choi, S.-H. Joo, B.-J. Lee, A. Podolskiy, M. Tikhonovsky and H.S. Kim: Mater. Lett. **202** (2017) 86-88.

88. E.D. Tabachnikova, A.V. Podolskiy, V.Z. Bengus, S.N. Smirnov, M.I. Bidylo, K. Csach, J. Miskuf, L.R. Saitovac, I.P. Semenova and R.Z. Valiev: Mater. Sci. Eng. A **503** (2009) 106–109.

89. E.D. Tabachnikova, V.Z. Bengus, A.V. Podolskiy, S.N. Smirnov, V.D. Natsik, K. Csach, J. Miskuf, D.V. Gunderov and R. Valiev: Rev. Adv. Mater. Sci. **10** (2005) 229-234.

90. Yu.O. Semerenko, E.D. Tabachnikova, T.V. Hryhorova, S.E. Shumilin, Yu.O. Shapovalov, H.S. Kim, J. Moon and H. Kwon: Metallofizika and Noveishie Tekhnol. **43** (2021) 273–287 (in Ukrainian).

91. A.V. Podolskiy, E.D. Tabachnikova, M.A. Tikhonovsky, M.J. Zehetbauer and E. Schafler: Low Temp. Phys. **44** (2018) 976-982.

92. H. Shahmir, E. Tabachnikova, A. Podolskiy, M. Tikhonovsky and T.G. Langdon: J. Mater. Sci. **53** (2018) 11813-11822.

93. J. Moon, Y. Qi, E. Tabachnikova, Yu. Estrin, W.-Mi. Choi, S.-H. Joo, B.-J. Lee, A. Podolskiy, M. Tikhonovsky and H.S. Kim: Sci. Rep. **8** (2018) 1-12.

94. T.V. Hryhorova, S.E. Shumilin, Yu.O. Shapovalov, Yu.O. Semerenko, O.D. Tabachnikova, M.A. Tikhonovsky, A.S. Tortika, M.I. Zehetbauer and E. Schafler: J. V.N. Karazin Kharkiv Natl. Univ. Phys. **32** (2020) 41– 48 [in Ukraine].

95. Yu.O. Shapovalov, O.D. Tabachnikova, M.A. Tikhonovsky, A.V. Levenets, M.I. Zehetbauer and E. Schafler: J. V.N. Karazin Kharkiv Natl. Univ. Phys. **32** (2020) 59-64 [in Ukraine].

96. A.V. Rusakova, L.S. Fomenko, S.N. Smirnov, A.V. Podolskiy, Y.O. Shapovalov, E.D. Tabachnikova, M.A. Tikhonovsky, A.V. Levenets, M.J. Zehetbauer and E. Schafler: Mater. Sci. Eng. A **828** (2021) 142116.

97. A.V. Levenets, H.V. Rusakova, L.S. Fomenko, Yi. Huang, I.V. Kolodiy, R.L. Vasilenko, E.D. Tabachnikova, M.A. Tikhonovsky and T.G. Langdon: Low Temp. Phys. **48** (2022) 629-640.

98. E.D. Tabachnikova, V.Z. Bengus, A.V. Podolskiy, S.N. Smirnov, D.V. Gunderov and R.Z. Valiev: Materials Science Forum **503-504** (2006), pp 633-638 [online at http://www.scientific.net, Trans Tech Publications, Switzerland]

99. E.D. Tabachnikova, V.Z. Bengus, A.V. Podolskiy, S.N. Smirnov, K. Csach, J. Miskuf, L.R. Saitova, I.P. Semenova and R.Z. Valiev: Int. J. Mech. Mater. Des. **4** (2008) 189–95.

100. V.A. Moskalenko, A.R. Smirnov and A.V. Moskalenko: Low Temp. Phys. **35** (2009) 905-907.

101. V.A. Moskalenko, V.I. Betekhtin, B.K. Kardashev, A.G. Kadomtsev, A.R. Smirnov, R.V. Smolyanets and M.V. Narykova: Phys. Solid State **56** (2014) 1590–1596.

102. V.A. Moskalenko, A.R. Smirnov, Yu.M. Plotnikova, I.S. Braude and R.V. Smolianets: Mater. Sci. Eng. A **700** (2017) 707-713.

103. S.V. Zherebtsov, G.S. Dyakonov, A.A. Salem, V.I. Sokolenko, G.A. Salishchev and S.L. Semiatin: Acta Mater. **61** (2013) 1167–1178.

104. E.D. Tabachnikova, A.V. Podolskiy, S.N. Smirnov, M.A. Tikhonovsky, P.A. Khaimovich, N.I. Danylenko and S.A. Firstov: Bulletin of KhNU series “Physics” **28** (2018) 63-67.

105. U. Zwicker: *Titan und Titanlegierungen*, (Springer-Verlag, Berlin, 1974).

106. R.Z. Valiev, R.K. Islamgaliev and I.V. Alexandrov: Prog. Mater. Sci. **45** (2000) 103–189.

107. E.D. Tabachnikova, V.Z. Bengus, V.V. Stolyarov, G.I. Raab, R.Z. Valiev, J. Miskuf and K. Csach: Mater. Sci. Eng. A **309-310** (2001) 524-527.

108. V.Z. Bengus, E.D. Tabachnikova, V.D. Natsik, J. Miskuf, K. Csach, V.V. Stolyarov and R.Z. Valiev: Low Temp. Phys. **28** (2002) 864-874.

109. E.D. Tabachnikova, V.Z. Bengus, V.D. Natsik, A.V. Podolskiy, S.N. Smirnov, R.Z. Valiev, V.V. Stolyarov and I.V. Alexandrov: *Nanomaterials by Severe Plastic Deformation*, (J. Wiley VCH, Weinheim, 2004) pp. 207.

110. V. Bengus, S. Smirnov, E. Tabachnikova, V. Romanchenko, S. Khomenko, D. Gunderov, V. Stolyarov and R. Valiev: Metal Phys. Adv. Technol. **26** (2004) 1483-1492 (in Russian).

111. E. Tabachnikova, V. Bengus, V. Natsik, K. Csach, J. Miskuf, V. Stolyarov and R. Valiev In: Y.T. Zhu, V. Varyukhin, (Eds.): *Nanostructured Materials by High-Pressure Severe Plastic Deformation*, (Springer, Dordrecht, 2006) pp. 259–263.

112. A.V. Podolskiy, S.N. Smirnov, E.D. Tabachnikova, V.Z. Bengus, A.N. Velikodny, M.A. Tikhonovsky, B. Bonarski, C. Mangler and M.J. Zehetbauer, Low Temp. Phys. **37** (2011) 609–617.

113. L.T. Zhang, K. Ito, V.K. Vasudevan and M. Yamaguchi: Acta Mater. **49** (2001) 751–758.

114. L.T. Zhang, K. Ito, V.K. Vasudevan and M. Yamaguchi: Mater. Sci. Eng. A **329-331** (2002) 362–366.

115. T.T. Ueda, M. Tsukahara, Y. Kamiya and S. Kikuchi: J. Alloys. Compd. **386** (2005) 253–257.

116. D.K. Yang, P.D. Hodgson and C.E. Wen: Scripta Mater. **63** (2010) 941-944.

117. J.P. Hirth and J. Lothe: *Theory of dislocations*, (Wiley, New York, 1982) pp. 231.

118. R.Z. Valiev and T.G. Langdon: Prog. Mater. Sci. **51** (2006) 881–981.

119. R.Z. Valiev, Y. Estrin, Z. Horita, T.G. Langdon, M.J. Zehetbauer and Y.T. Zhu: JOM **58** (2006) 33–39.

120. V.M. Segal, V.I. Reznikov, A.E. Drobyshevskiy and V.I. Kopylov: Russ Metall. **1** (1981) 99–105.

121. V.M. Segal: *Materials preparation for following processing*, USSR Invention Certificate **575** (1977) 892.

122. R. Lapovok, A. Molotnikov, Y. Levin, A. Bandaranayake and Y. Estrin: J. Mater. Sci. **47** (2012) 4589–4594.

123. H. Shahmira, M. Nili-Ahmadabadi, A. Shafiee and T.G. Langdon: Mater. Sci. Eng. A **718** (2018) 468–476.

124. H. Shahmir, M. Nili-Ahmadabadi, A. Shafiee, M. Andrzejczukc, M. Lewandowska and T.G. Langdon: Mater. Sci. Eng. A **725** (2018) 196–206.

125. X. Liu, H. Ding, Y. Huang, X. Bai, Q. Zhang, H. Zhang, T.G. Langdon and J. Cui: J. Alloys Compd. **867** (2021) 159063.

126. R.B. Figueiredo, W. Wolf and T.G. Langdon: J. Mater. Res. Technol. **20** (2022) 2358-2368.

127. H. Shahmir, M.S. Mehranpour, S. Amir, A. Shams, C.S. Lee and T.G. Langdon: High Entropy Alloys & Materials (2022) 1–12.

128. K. Edalati and Z. Horita: Mater. Sci. Eng. A **652** (2016) 325–352.

129. A.V. Levenets, H.V. Rusakova, L.S. Fomenko, Y. Huang, I.V. Kolodiy, R.L. Vasilenko, E.D. Tabachnikova, M.A. Tikhonovsky and T.G. Langdon: Low Temp. Phys. **48** (2022) 629–640.

130. A.P. Zhilyaev and T.G. Langdon: Prog. Mater. Sci. **53** (2008) 893–979.

131. V.D. Blank, M.Y. Popov and B.A. Kulnitskiy: Mater Trans. **60** (2019) 1500–1505.

132. A.V. Stolbovsky, V.V. Popov, E.N. Popova and V.P. Pilyugin: Bull. Russ. Acad. Sci. Phys. **78** (2014) 908-916.

133. Y. Ikoma, K. Kumano, K. Edalati, K. Saito, Q. Guo and Z. Horita: Philos. Mag. Lett. **97** (2017) 27-34.

134. A.P. Zhilyaev and T.G. Langdon: J. Mater. Sci. **49**, (2014) 6529–6535.

135. Y. Huang, M. Lemang, N.X. Zhang, P.H.R. Pedro and T.G. Langdon: Mater. Sci. Eng. A **656**, (2016) 55–66.

136. S. Turtze and V.-T. Kuokkala: Acta Mater. **58**, (2010) 5129–5141.

137. A.J. Zaddach, C. Niu, C.C. Koch & D.L. Irving: JOM **65**, (2013) 1780–1789.

138. R.J. Asaro and S. Suresh: Acta Mater. **53** (2005) 3369-3392.

139. M. Kato: Mater. Sci. Eng. A **516** (2009) 276-282.

140. G. Saada and T. Kruml: Acta Mater. **59** (2011) 2565-2574.

141. E.D. Tabachnikova, A.V. Podolskiy, S.N. Smirnov, I.A. Psaruk, Z. Bengus, H. Li, L. Li, H. Chu and P.K. Liao: Low Temp. Phys. **38** (2012) 239-247.

142. E.D. Tabachnikova, A.V. Podolskiy, S.N. Smirnov, I.A. Psaruk and P.K. Liao: Mater. Sci. Eng. **63** (2014) 1-12.

143. E.D. Tabachnikova, Yu.O. Shapovalov, S.N. Smirnov, V.F. Gorban', N.A. Krapivka and S.A. Firstov: Low Temp. Phys. **46** (2020) 958-968.

144. E.D. Tabachnikova, M.A. Laktionova, Yu.A. Semerenko, S.E. Shumilin, A.V. Podolskiy, M.A. Tikhonovsky, J. Miskuf and K. Csach: Low Temp. Phys. **43** (2017) 1108-1118.

145. A.V. Podolskiy, E. Schafler, E.D. Tabachnikova, M.A. Tikhonovsky and M.J. Zehetbauer: Low Temp. Phys. **44** (2018) 976-982.

146. V.A. Moskalenko, R.V. Smolianets, V.D. Natsik and Yu.M. Pohribna, Low Temp. Phys. **49** (2023) 268–276.

147. A.G. Evans and R. Rawlings: Phys. Status Solidi **34** (1969) 9-31.

148. V.N. Kovaleva, V.A. Moskalenko and V.D. Natsik: Philos. Mag. A **70** (1994) 423-438.

149. E.D. Tabachnikova, A.V. Podolskiy, S.N. Smirnov, I.A. Psaruk and P.K. Liao: Low Temp. Phys. **40**, (2014), 1104-1111.

150. A. Seeger: J. Phys. (Paris) Colloq. **42(C5)** (1981) 201.

151. J. Friedel: *Dislocation*, (Pergamon, London, 1964) pp. 512.

152. E.J. Pickering, H.J. Stone and N.G. Jones: Mat. Sci. Eng. A **645** (2015) 65-71.

153. Y. Estrin, N.V. Isaev, S.V. Lubenets, S.V. Malykhin, A.T. Pugachov, V.V. Pustovalov, E.N. Reshetnyak, V.S. Fomenko, L.S. Fomenko, S.E. Shumilin, M. Janecek and R.J. Hellmig: Acta Mater. **54** (2006) 5581-5590.

154. N.V. Isaev, T.V. Grigorova, S.E. Shumilin, S.S. Polishchuk and O.A. Davydenko, Low Temp. Phys. **43** (2017) 1420-1426.

155. Y. Estrin, V. Fomenko, T. Grigorova, N. Isaev, V. Pustovalov, S. Shumilin and M. Janecek: Adv. Eng. Mater. **11** (2009) 9-15.

156. S. Shumilin, M. Janecek, N. Isaev, P. Homola and R. Kral, Adv. Eng. Mater. **14** (2012) 35-38.

157. S.E. Shumilin, N.V. Isaev, P.A. Zabrodin, V.S. Fomenko, T.V. Grigorova and V.G. Geidarov, Acta Phys. Pol. A **128** (2015) 536-539.

158. S. Shumilin, M. Janecek, N. Isaev, P. Minarik and R. Kral: Adv. Eng. Mater. **15** (2013) 352-357.

159. N. Isaev, S. Shumilin, P. Zabrodin, M. Janecek and J. Stráská: Acta Physica Polonica A **134** (2018) 662-666.

160. E.D. Tabachnikova, M.A. Laktionova, Yu.A. Semerenko, S.E. Shumilin, A.V. Podolskiy, M.A. Tikhonovsky, J. Miskuf and K. Csach, Low Temp. Phys.**43** (2017) 1108-1118.

161. J. Moon, E. Tabachnikova, S. Shumilin, T. Hryhorova, Y. Estrin, J. Brechtl, P. Liaw, W. Wang, K. Dahmen, A. Zargaran, J.W. Bae, H.S. Do, B.-J. Lee and H.S. Kim: Mater. Today **50** (2021) 55-68.

162. E.D. Tabachnikova, T.V. Hryhorova, S.E. Shumilin, I.V. Kolodiy, Yu.O. Shapovalov, Yu.O. Semerenko, S.N. Smirnov, I.V. Kashuba, M.A. Tikhonovsky, M.J. Zehetbauer, and E. Schafler: Low Temp. Phys. **48** (2021) 845-852.

163. E.D. Tabachnikova, S.E. Shumilin, T.V. Hryhorova, Yu.O. Shapovalov, Yu.A. Semerenko, S.N. Smirnov, I.V. Kolodiy, M.A. Tikhonovsky, M.J. Zehetbauer and E. Schafler: Proc. of "ICSMA19", (Metz France, 2022).

164. J. Moon, E. Tabachnikova, S. Shumilin, T. Hryhorova, Y. Estrin, J. Brechtl, P.K. Liaw, W. Wang, K.A. Dahmen and H.S. Kim: Phys. Rev. Mater. **5** (2021) 083601.

165. I.N. Kuzmenko, V.V. Pustovalov and S.E. Shumilin: PTE **1** (1988) 196 [in Russian].

166. V.V. Pustovalov and V.S. Fomenko: *Plactic deformation of crystals at low temperatures*, (Naykova Dymka, Kyiv, 2012) pp. 357 [in Russian].

167. N.V. Isaev, V.D. Natsik, V.V. Pustovalov, V.S. Fomenko and S.E. Shumilin: Low Temp. Phys. **31** (2005) 898-906.

168. N.V. Isaev, V.D. Natsik, V.V. Pustovalov, I.A. Shepel and S.E. Shumilin: Sov. J. Low Temp. Phys. **18** (1992) 641.

169. V.I. Alshits and V.I. Indenbom: *Mechanisms of dislocations drag*, in: F.R.N. Nabarro, Eds.: *Dislocations in solids*, (Elsevier Science Pub. Co., North-Holland Amsterdam, 1986) pp. 43-111.

170. V.V. Pustovalov: Low Temp. Phys. **34** (2008) 683-723.

171. A. Seeger: Philos. Mag. **46** (1955) 1194-1217.

172. A.V. Granato: Phys. Rev. B **4** (1971) 2196-2201.

173. M.I. Kaganov, V.Y. Kravchenko and V.D. Natsik: Uspekhi Fizicheckikh Nauk **111** (1973) 655-682 [in Russian].

174. V.S. Bobrov and M.A. Lebedkin: Fizika Tverdogo Tela, **35** (1993) 1881-1889 [in Russian].

175. V.S. Bobrov and M.A. Lebedkin: Fizika Tverdogo Tela **31** (1989) 120-126 [in Russian].

176. B.Ya. Farber, N.S. Sidorov, V.I. Kulakov, Yu.A. Iunin, A.N. Izotov, G.A. Emel'chenko, V.S. Bobrov, L.S. Fomenko, V.D. Natsik and S.V. Lubenets: Superconductivity **4** (1991) 2394-2403.

Captions List

Table 1 Twin thickness and spacing between twins as a function of thickness strain during rolling at 293 and 77 K. [103)]

Table 2 Microhardness of initial coarse-grained Ti and nanostructured Ti (after HPT processing at 2 GPa, achieved at temperatures of processing and of subsequent annealing as indicated) [16)].

Table 3 Values of the theory parameters obtained as a result of thermal activation analysis of experimental data for alloys considered in papers. [142-146)]

Table 4 Mechanical characteristics of UFG copper in different structural states (A, B, C) and coarse-grained HEA $Fe_{50}Mn_{30}Co_{10}Cr_{10}$ (TRIP) and $Fe_{40}Mn_{40}Co_{10}Cr_{10}$ (TWIP) in the temperature range 295–0.5 K. [154, 163, 164)]

Fig. 1 TEM micrographs of CP Ti rolled at 77 K to a true thickness strain ε_{th} of 2.66 (a, b). [103)]

Fig. 2 Typical dark field transmission electron microscopy images and correspondent diffraction patterns of the Ti Grade 2 structure: state 2 (after ECAP) (a); state 7 (ECAP + QHE at 77 K) (b). [104)]

Fig. 3 Representative microstructures of the CP-Ti samples processed under different ECAP conditions: (a) 1 pass at 77 K, (b) 1 pass at 300 K, (c) 1 pass at 575 K, (d) 2 passes at 77 K, (e) 2 passes at 300 K, (f) 2 passes at 575 K, (g) 3 passes at 77 K, (h) 3 passes at 300 K and (i) 3 passes at 575 K. Inset in each figure represents the corresponding electron diffraction patterns.

7)

Fig. 4 Temperature dependence of yield stress in compression for coarse-grained and different structural states of nanostructured HPT Ti. [16)]

Fig. 5 Deformation curves from compression at temperatures 300, 77, 4.2 K: (a) – coarse-grained Zr; (b) – nanostructured Zr (HPT at 4 GPa, 300 K); (c) – nanostructured Zr (HPT at 2 GPa, 300 K); (d) - nanostructured Zr (HPT at 4 GPa, 300 K + annealing); (e) – nanostructured Zr (HPT at 2 GPa, 77 K). [14)]

Fig. 6 Comparison of the temperature dependence of the yield strength $\sigma_{0.2}$ under uniaxial compression at a rate of 3×10^{-4} s^{-1} in the CoCrFeMnNi alloy in the coarse-grained (▲) state (grain size ~ 4 μm[79)]) and nanostructural states: after HPT at 300 K (●) and after cryo-HPT (★) (grain size between 40 and 80 nm, very few grains with sizes larger than 200 nm, at a pressure of 6 GPa and torsion strain γ=25).[96)]

Fig. 7 Hardness of CoCrFeNiMn HEA after HPT processing up to γ=180: a) microhardness (load 1.5 N) measured at 300 K after HPT processing at 300 K and after cryo-HPT processing at 6 GPa for various annealing times at 300 K; b) macrohardness (load 49 N) measured in liquid nitrogen at 77 K after HPT processing at 300 K and cryo-HPT processing, both done at 6 GPa.[79)]

Fig. 8 Temperature dependences of the average microhardness value of Cantor alloy obtained at P = 1.5 N: ■ - initial coarse-grained sample, ○ - sample subjected to HPT at 299 K, ● - sample subjected to cryo-HPT.[96)] The procedure for measuring the microhardness in the temperature range 77-290 K is given in.[176)]

Fig. 9 A schematic diagram illustrating the microstructural evolution of $Co_{20}Cr_{26}Fe_{20}Mn_{20}Ni_{14}$ alloy. The microstructural evolution of $Co_{20}Cr_{26}Fe_{20}Mn_{20}Ni_{14}$ alloy which accommodates the stored strain energy during and after cryo-HPT.[93)]

Fig. 10 TEM images of CoCrFeNiMn HEA after HPT at different temperatures: (a) T = 300 K (bright field), (b) T = 77 K (bright field) with the corresponding diffraction patterns in the inside, (c) X-ray diffraction patterns after HPT at 77 K and 300 K, black circle - local phase transformations during HPT at 77 K.[79)]

Fig. 11 Temperature dependences of flow stress $\tau_2(T)$, strain rate sensitivity of deforming stress $\Delta\tau/\Delta\ln\dot{\varepsilon}_\alpha$ at strain $\varepsilon \sim 2\%$ for nanocrystalline (NC) (a) and coarse-grained (CG) (b) states of the alloy under study. The solid lines represent the theoretical dependences (curve 1) and (curve 2) for Ni-18.75 at.% Fe alloy.[142)]

Fig. 12 Activation volume as a function of effective stress τ^*. Theoretical dependences $V(\tau^*)$are indicated by solid lines; formal extrapolation of theoretical dependences $V(\tau^*)$ for the NC and for the CG alloys.[142)]

Fig. 13 True stress–strain curves for the $Co_{17.5}Cr_{12.5}Fe_{55}Ni_{10}Mo_5$ alloy at different temperatures and temperature dependence of the yield strength and the elongation to failure (as a measure of ductility) of the alloy exhibiting anomalies below a critical temperature set notionally at 4.2 K, average grain size 3.82 ± 1.82 μm.[161)]

Fig. 14 Temperature dependence of the yield strength $\sigma_{0.2}$ for coarse-grained the $Fe_{40}Mn_{40}Co_{10}Cr_{10}$ (TWIP) (a) and $Fe_{50}Mn_{30}Co_{10}Cr_{10}$ (TRIP) (b) in the range 0.5–80 K.[163)]

Tables

Table 1 Twin thickness and spacing between twins as a function of thickness strain during rolling at 293 and 77 K.[103)]

ε_{th}	Twin thickness (μm)		Spacing between twins (μm)	
	293 K	77 K	293 K	77 K
0.1	2.3	1.2	7.9	3.5
0.22	1.9	1.0	6.5	3.0
0.36	2.2	0.7	5.9	2.8

Table 2 Microhardness of initial coarse-grained Ti and nanostructured Ti (after HPT processing at 2 GPa, achieved at temperatures of processing and of subsequent annealing as indicated).[16)]

	Coarse-grained Ti	HPT Ti, 77 K	HPT Ti, 300 K	HPT Ti, 300 K + anneal. at 425 K	HPT Ti, 300 K + anneal. at 485 K	HPT Ti, 300 K + anneal. at 545 K	CP Ti coarse-grained[134)]	CP Ti HPT[134)]
Vickers microhardness, HV	97	278	248	245	205	145	140	265

Table 3 Values of the theory parameters obtained as a result of thermal activation analysis of experimental data for alloys considered in papers.[142-146)]

Alloy	Grain size	p	q	τ_{i0}, MPa	τ_{c0}, MPa	H_{00}, eV	T_{00}, K	A
$Al_{0.5}CoCrCuFeNi$[144)]		0.6	1.08	170	104	0.65	400	19
$CrMnFeCoNi_2Cu$[143)]		2/3	1.6	408	206	0.82	382	25
Ni-18.75%Fe[142)]	CG	0.518	1.056	942.62	715.49	1.005	656.5	17.76
	NC	2/3	1.12		674.78	0.787	514.1	17.76
	CG	2/3	1.712	139.40	70.59	0.669	442.7	17.55
CoCrFeNiMn[145)]	NC		1.4	627	512	0.65	384	19.51
	CG		1.71	145	134	0.63	353	20.80
Ti[146)]	35 nm	1	3/2	347	415	1.39	1350	12
	45 nm	1	3/2	330	340	1.24	1200	12
	2 μm	1	3/2	75	270	1.2	1000	14

Table 4 Mechanical characteristics of UFG copper in different structural states (A, B, C) and coarse-grained HEA $Fe_{50}Mn_{30}Co_{10}Cr_{10}$ (TRIP) and $Fe_{40}Mn_{40}Co_{10}Cr_{10}$ (TWIP) in the temperature range 295–0.5 K[153, 162, 163].

Materials	**Mechanical characteristic**	**Temperature, K**			
		295	**77**	**4.2**	**0.5**
Cu tape A – the average grain size of approximately 1 μm, containing a high density of tangled dislocations	Yield strength, MPa	300		422	396
	Ultimate strength, MPa	330		517	516
	Elongation, %	2		26	31
Cu tape B - the mixed structure: grains 0.5–1 μm in size with a high density of dislocations inside (30%) and relatively large dislocation-free grains 1–10 μm in size, with many twins (70%)	Yield strength, MPa	290			400
	Ultimate strength, MPa	350			570
	Elongation, %	2			20
Cu type C - grain size in the range of 1-10 μm	Yield strength, MPa	180			243
	Ultimate strength, MPa	210			492
	Elongation, %	12			27
$Fe_{40}Mn_{40}Co_{10}Cr_{10}$	Yield strength, MPa	188	410	576	541
	Ultimate strength, MPa	510	1166	1226	1778
	Elongation, %	59	62	60	57
$Fe_{50}Mn_{30}Co_{10}Cr_{10}$	Yield strength, MPa	230	450	606	536
	Ultimate strength, MPa	758	1384	1513	1274
	Elongation, %	50	48	47	54

Figures

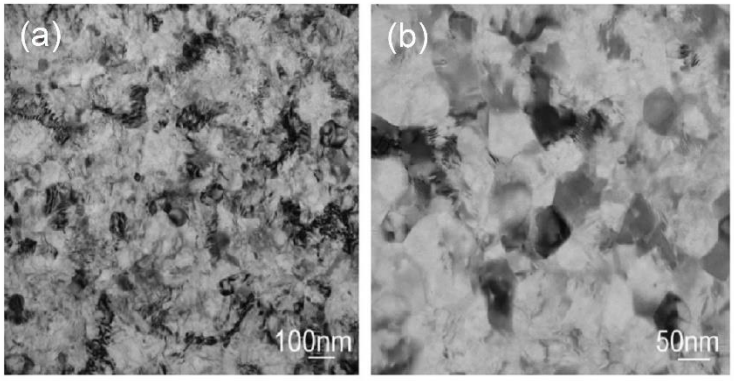

Fig. 1 TEM micrographs of CP Ti rolled at 77 K to a true thickness strain ε_{th} of 2.66 (a, b). [103)]

Monochrome Print

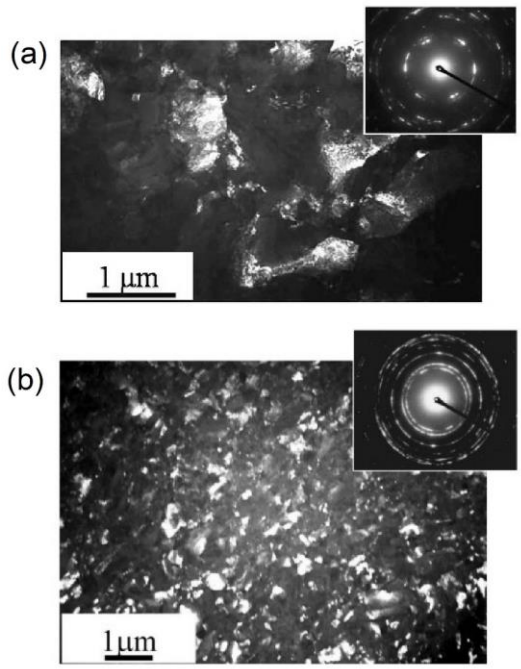

Fig. 2 Typical dark field transmission electron microscopy images and correspondent diffraction patterns of the Ti Grade 2 structure: state 2 (after ECAP) (a); state 7 (ECAP + QHE at 77 K) (b).[104)]

Monochrome Print

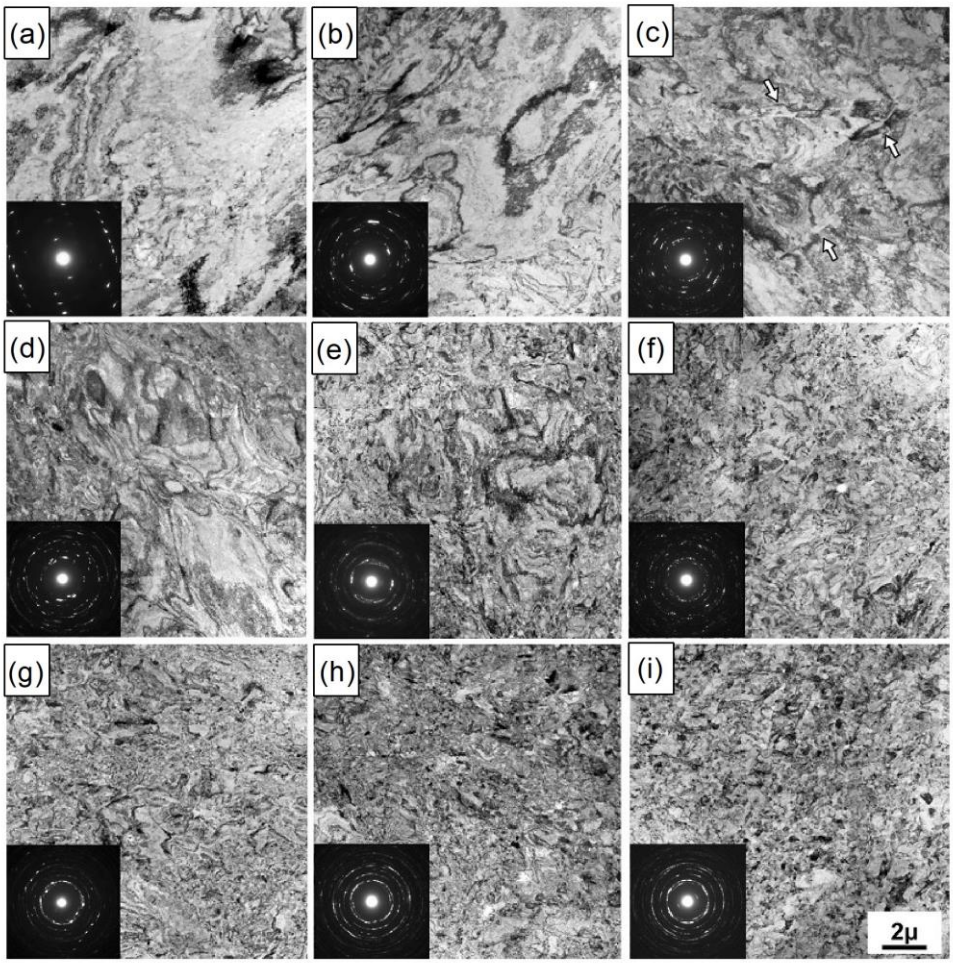

Fig.3 Representative microstructures of the CP-Ti samples processed under different ECAP conditions: (a) 1 pass at 77 K, (b) 1 pass at 300 K, (c) 1 pass at 575 K, (d) 2 passes at 77 K, (e) 2 passes at 300 K, (f) 2 passes at 575 K, (g) 3 passes at 77 K, (h) 3 passes at 300 K and (i) 3 passes at 575 K. Inset in each figure represents the corresponding electron diffraction patterns.[7)]

Monochrome Print

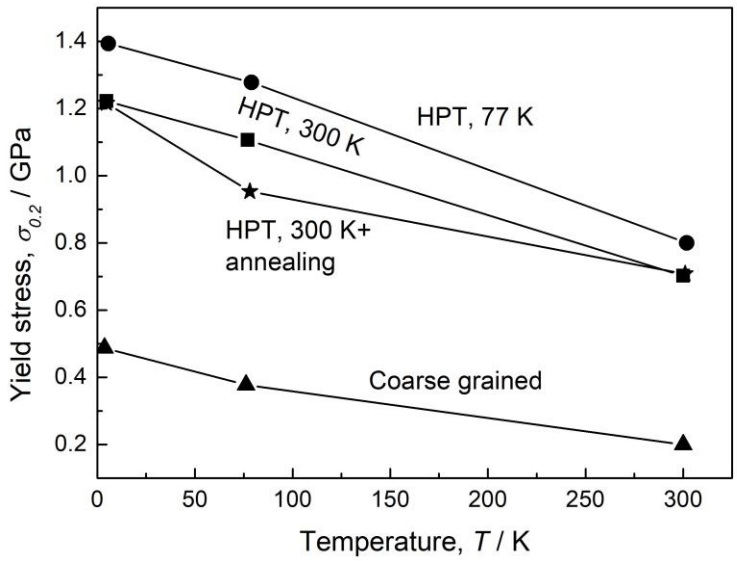

Fig. 4 Temperature dependence of yield stress in compression for coarse-grained and different structural states of nanostructured HPT Ti.[16)]

Monochrome Print

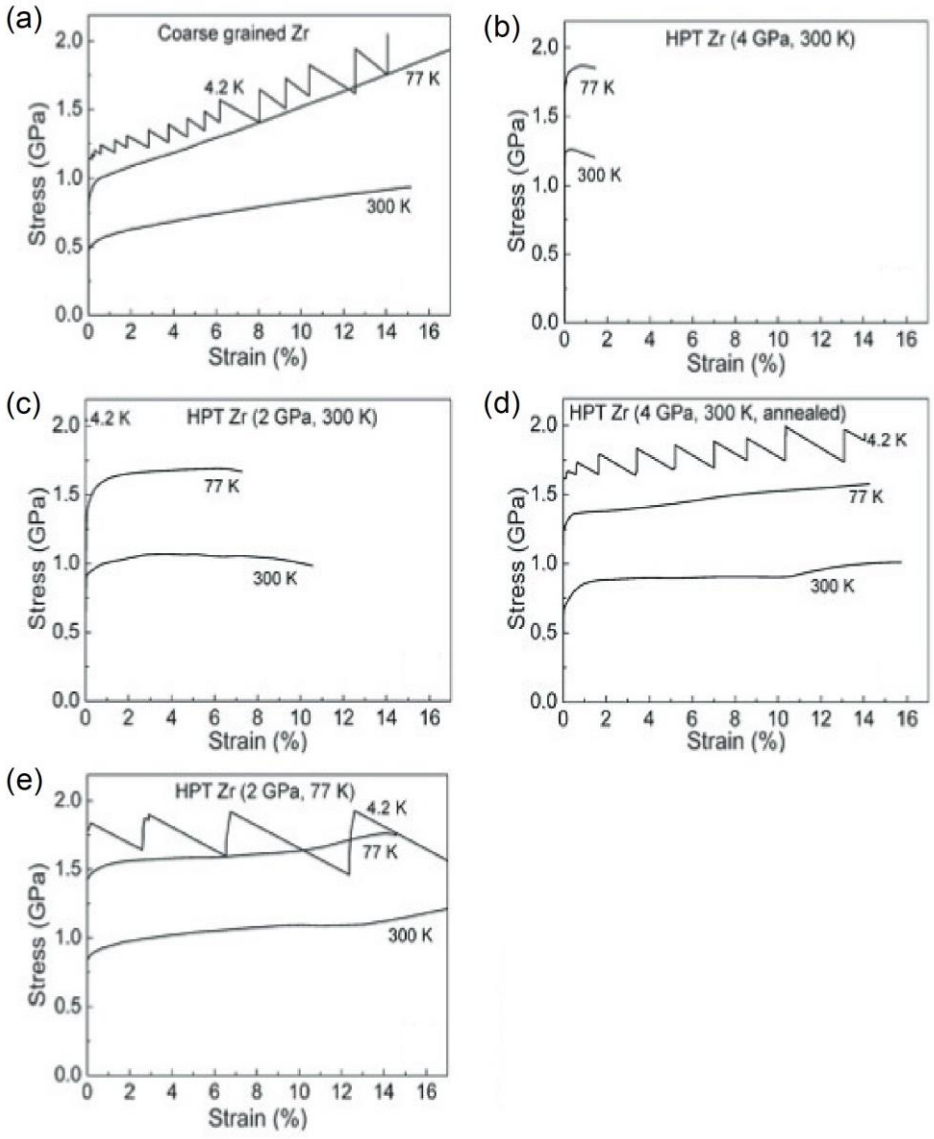

Fig. 5 Deformation curves from compression at temperatures 300, 77, 4.2 K: (a) – coarse-grained Zr; (b) – nanostructured Zr (HPT at 4 GPa, 300 K); (c) – nanostructured Zr (HPT at 2 GPa, 300 K); (d) - nanostructured Zr (HPT at 4 GPa, 300 K + annealing); (e) – nanostructured Zr (HPT at 2 GPa, 77 K).[14)]

Monochrome Print

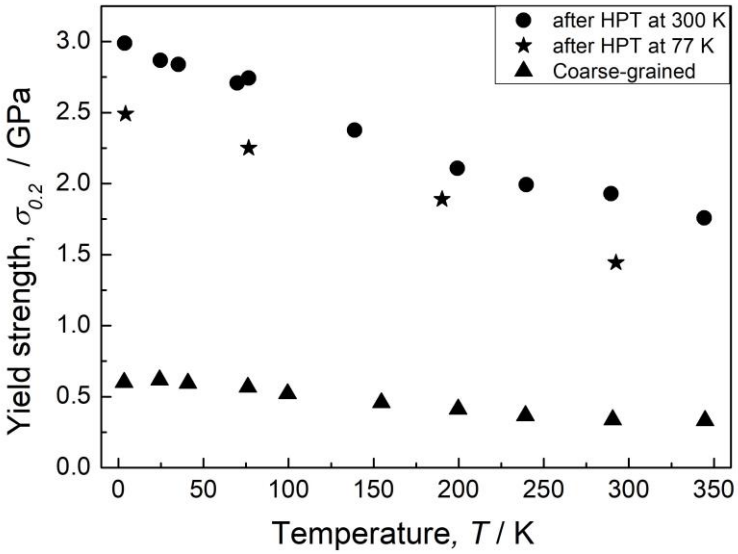

Fig. 6 Comparison of the temperature dependence of the yield strength $\sigma_{0.2}$ under uniaxial compression at a rate of 3×10^{-4} s^{-1} in the CoCrFeMnNi alloy in the coarse-grained (▲) state (grain size ~ 4 μm[79]) and nanostructural states: after HPT at 300 K (●) and after cryo-HPT (★) (grain size between 40 and 80 nm, very few grains with sizes larger than 200 nm, at a pressure of 6 GPa and torsion strain γ=25).[96]

Monochrome Print

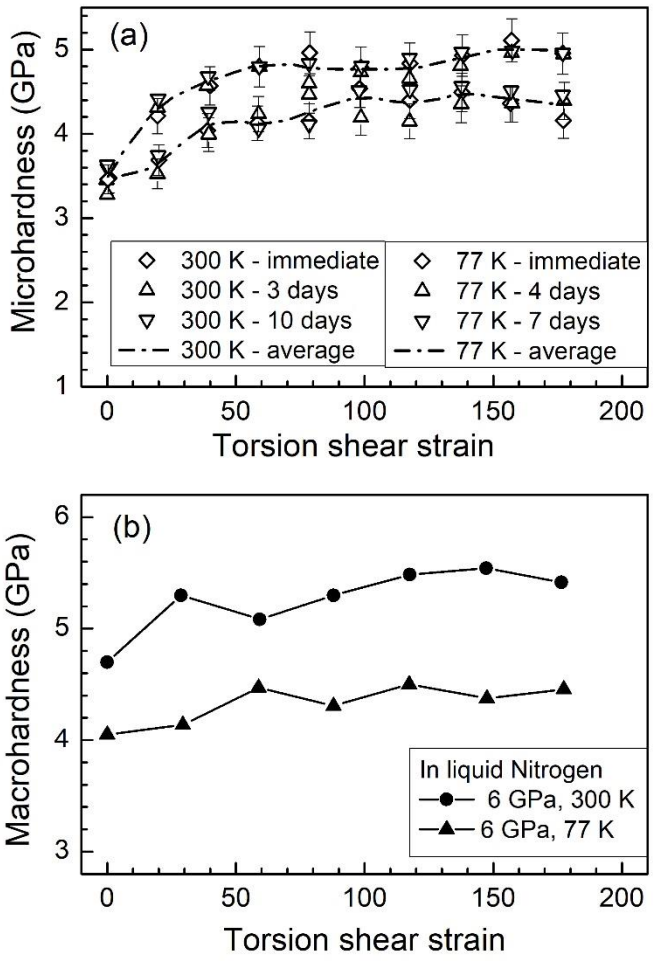

Fig. 7 Hardness of CoCrFeNiMn HEA after HPT processing up to γ=180: a) microhardness (load 1.5 N) measured at 300 K after HPT processing at 300 K and after cryo-HPT processing at 6 GPa for various annealing times at 300 K; b) macrohardness (load 49 N) measured in liquid nitrogen at 77 K after HPT processing at 300 K and cryo-HPT processing, both done at 6 GPa.[79)]

Monochrome Print

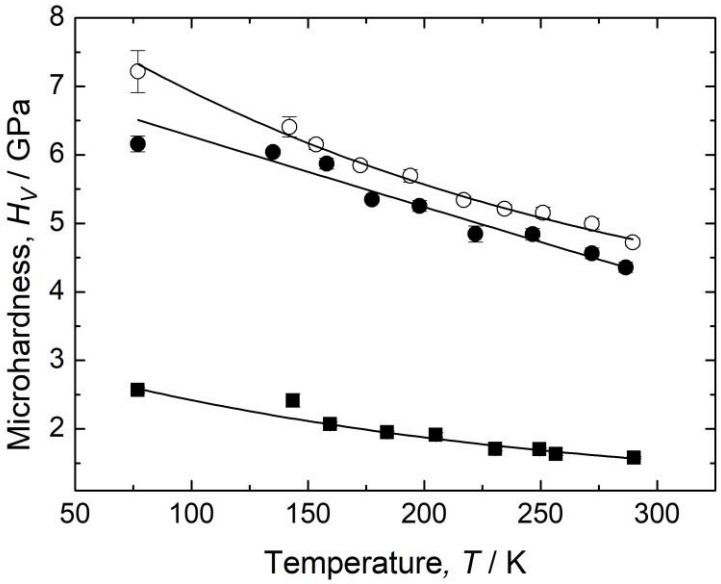

Fig. 8 Temperature dependences of the average microhardness value of Cantor alloy obtained at P = 1.5 N: ■ - initial coarse-grained sample, ○ - sample subjected to HPT at 299 K, ● - sample subjected to cryo-HPT.[96)] The procedure for measuring the microhardness in the temperature range 77-290 K is given in.[176)]

Monochrome Print

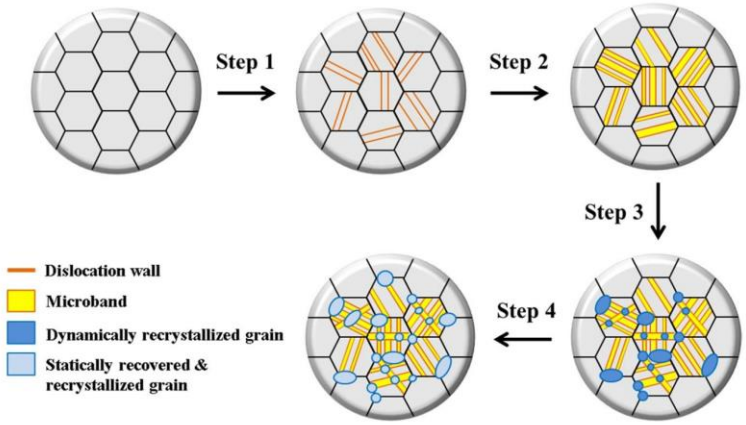

Fig. 9 A schematic diagram illustrating the microstructural evolution of $Co_{20}Cr_{26}Fe_{20}Mn_{20}Ni_{14}$ alloy. The microstructural evolution of $Co_{20}Cr_{26}Fe_{20}Mn_{20}Ni_{14}$ alloy which accommodates the stored strain energy during and after cryo-HPT.[93)]

Color Print

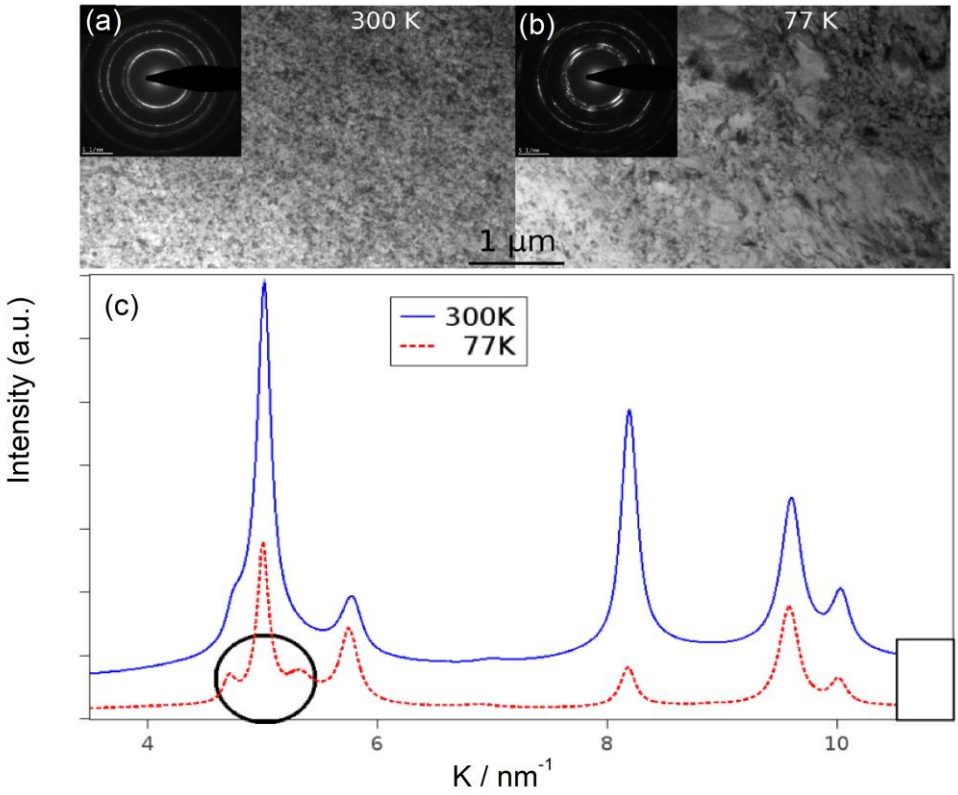

Fig. 10 TEM images of CoCrFeNiMn HEA after HPT at different temperatures: (a) T = 300 K (bright field), (b) T = 77 K (bright field) with the corresponding diffraction patterns in the inside, (c) X-ray diffraction patterns after HPT at 77 K and 300 K , black circle - local phase transformations during HPT at 77 K.[79)]

Color Print

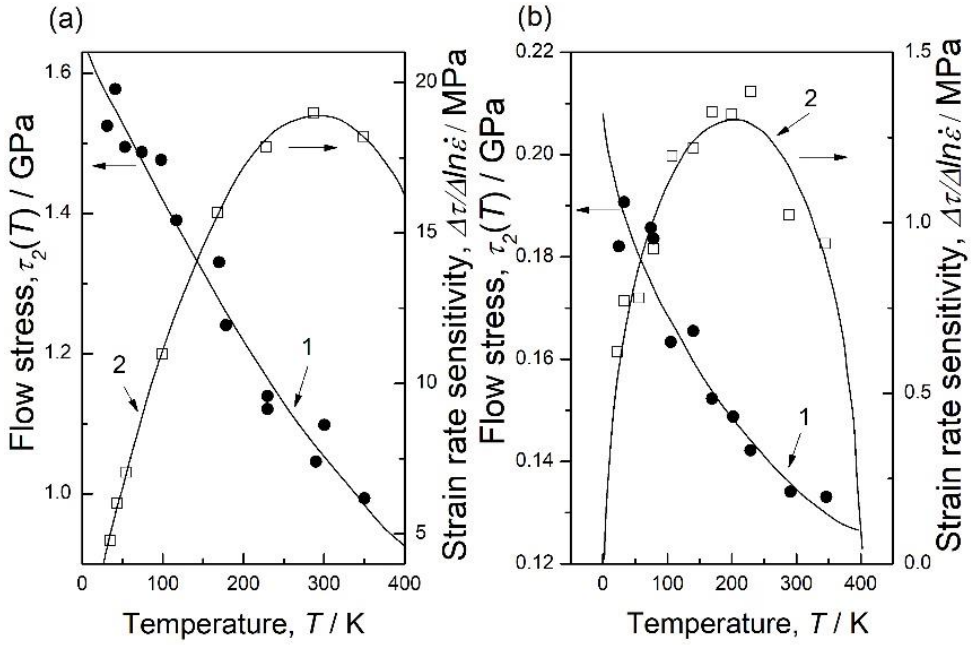

Fig. 11 Temperature dependences of flow stress $\tau_2(T)$, strain rate sensitivity of deforming stress $\Delta\tau/\Delta\ln\dot{\varepsilon}_\alpha$ at strain ε ~ 2% for nanocrystalline (NC) (a) and coarse-grained (CG) (b) states of the alloy under study. The solid lines represent the theoretical dependences (curve 1) and (curve 2) for Ni-18.75 at.% Fe alloy.[142)]

Monochrome Print

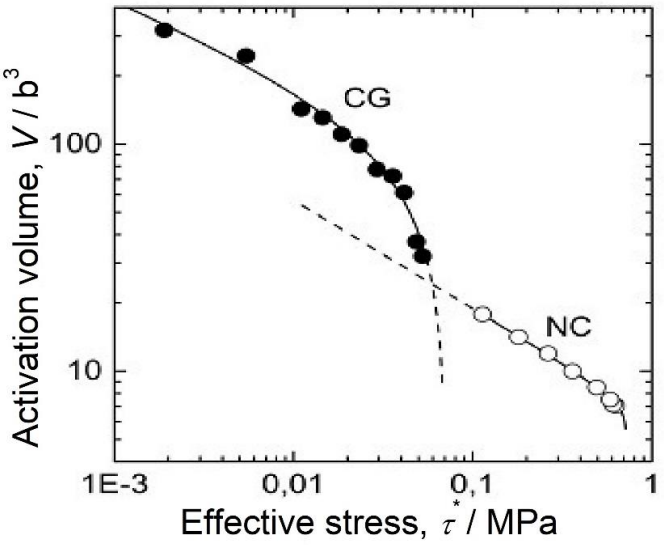

Fig. 12 Activation volume as a function of effective stress τ^*. Theoretical dependences $V(\tau^*)$are indicated by solid lines; formal extrapolation of theoretical dependences $V(\tau^*)$ for the NC and for the CG alloys.[142)]

Monochrome Print

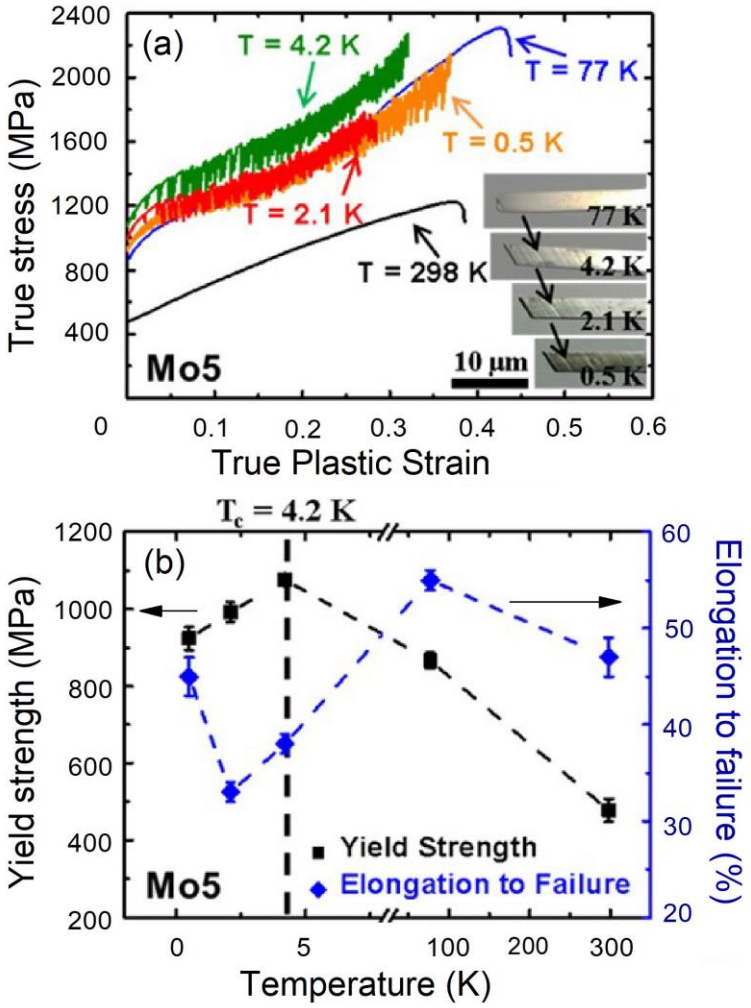

Fig. 13 True stress–strain curves for the $Co_{17.5}Cr_{12.5}Fe_{55}Ni_{10}Mo_5$ alloy at different temperatures and temperature dependence of the yield strength and the elongation to failure (as a measure of ductility) of the alloy exhibiting anomalies below a critical temperature set notionally at 4.2 K, average grain size 3.82 ± 1.82 μm.[161)]

Color Print

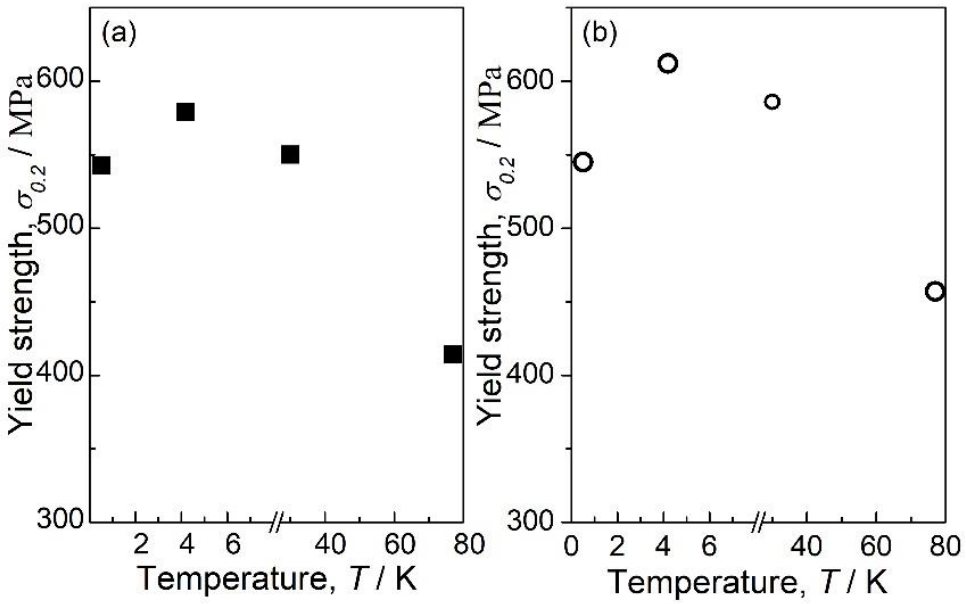

Fig. 14 Temperature dependence of the yield strength $\sigma_{0.2}$ for coarse-grained the $Fe_{40}Mn_{40}Co_{10}Cr_{10}$ (TWIP) (a) and $Fe_{50}Mn_{30}Co_{10}Cr_{10}$ (TRIP) (b) in the range 0.5–80 K.[163)]

Monochrome Print